

Bandgap optimization in locally resonant metamaterial plates: A comparative study of five lattice geometries for low-frequency wave attenuation

A.H.R. Ferreira^{a,*}, E.J.P. Miranda Jr.^{b,c,d}, A.M. Goto^a, J.M.C. Dos Santos^a

^a *University of Campinas, UNICAMP-FEM-DMC, Rua Mendeleyev, 200, CEP 13083-970, Campinas, SP, Brazil*

^b *Federal Institute of Maranhão, IFMA-PPGEM, CEP 65030-005, São Luís, MA, Brazil*

^c *Federal Institute of Maranhão, IFMA-EIB-DE, CEP 65010-030, São Luís, MA, Brazil*

^d *Vale Institute of Technology, ITV-MI, CEP 35400-000, Ouro Preto, MG, Brazil*

Abstract

The attenuation of low-frequency flexural waves (10 – 200)[Hz] represents a persistent challenge in structural engineering, requiring innovative solutions that balance efficiency, compactness, and weight constraints. This study presents the first systematic comparative analysis investigating the combined influence of lattice geometry and local resonator frequency on band gap formation in thin Kirchhoff-Love plates across five distinct periodic configurations. The primary objective is to establish quantitative design guidelines for optimal lattice-resonator arrangements in the critical low-frequency range for aerospace, automotive, and civil engineering applications. A comprehensive framework combining semi-analytical Plane Wave Expansion (PWE) and Extended Plane Wave Expansion (EPWE) methods with Finite Element Method (FEM) validation systematically analyzes 15 resonator frequencies across square, rectangular, triangular, honeycomb, and kagomé lattice configurations. The semi-analytical

*Corresponding author. Tel.: +55 11 958509690
Email address: a058899@dac.unicamp.br (A.H.R. Ferreira)

approach demonstrates computational efficiency improvements of two orders of magnitude over conventional FEM while maintaining accuracy within 5% of numerical predictions. Quantitative analysis reveals distinct performance hierarchies: triangular lattices achieve 35% superior relative bandwidth compared to square configurations (42.51% vs 31.40%) and demonstrate superior broadband characteristics; kagomé lattices provide up to 15 [dB] enhanced attenuation at low frequencies through triple-resonator coupling; honeycomb configurations offer balanced dual-band gap performance with coexisting frequency regions. A critical finding is the observation of two distinct complete band gaps in multi-resonator systems (honeycomb and kagomé), arising from in-phase and anti-phase resonator coupling modes, contrasting with single band gap behavior in single-resonator lattices (square, rectangular, triangular). Comprehensive bandwidth evolution analysis across all five lattice geometries establishes frequency-dependent performance maps for systematic design optimization. Bandwidth analysis employs infinite unit cell model predictions obtained through PWE/EPWE formulations. Finite plates consistently exhibit 40 – 50% bandwidth expansion beyond infinite domain predictions due to boundary-induced mode coupling effects. The research establishes the first quantitative hierarchy of lattice performance and provides engineers with systematic design guidelines for metamaterial plate optimization. This framework advances the field by bridging theoretical band gap predictions with practical finite plate performance, establishing essential tools for next-generation lightweight vibration isolation systems requiring efficient frequency-targeted vibration control.

Keywords: Locally resonant metamaterial, Flexural waves, Band gaps, Lattice configurations, Semi analytical method, Frequency-dependent optimization, Low-frequency vibration control.

¹ 1. Introduction

² Low-frequency noise and vibration mitigation represents a fundamental challenge in modern engineering applications, particularly within civil, naval, auto-

4 motive and aerospace systems [1–7]. Structures exposed to mechanical waves
5 in the 20 [Hz] to 200 [Hz] range—including aircraft fuselages, vehicle cabins, in-
6 dustrial machinery, and building floors—frequently experience unwanted reso-
7 nances and excessive structural vibrations [8, 9]. These phenomena precipitate
8 substantial economic and operational consequences: material fatigue reduces
9 component lifespans by 25-40% in aerospace applications, excessive vibrations
10 decrease industrial machinery efficiency by up to 15%, and noise-induced com-
11 fort degradation costs the aviation industry approximately \$3.2 billion annually
12 in passenger compensation and operational delays [10, 11].

13 Traditional passive noise control approaches, such as mass-damping systems
14 or viscoelastic coatings, impose severe design penalties: typical solutions re-
15 quire 150-300% mass increases to achieve 20 [dB] attenuation in the 20-200
16 [Hz] range, rendering them impractical for weight-sensitive applications where
17 every kilogram costs \$10,000-15,000 per flight hour in commercial aviation. Fur-
18 thermore, conventional treatments occupy 40-60% additional structural volume,
19 compromising payload capacity and architectural design flexibility [12–15]. Con-
20 sequently, the development of advanced acoustic metamaterials with tailored
21 bandgap properties has emerged as a critical technological imperative for achiev-
22 ing effective wave attenuation while maintaining compact, lightweight designs
23 that preserve operational performance and economic viability.

24 The conceptual foundations of wave propagation control in structured materi-
25 als trace back to pioneering developments in photonics during the late 1980s.
26 The seminal works of Yablonovitch and John in 1987 [16, 17] introduced the
27 revolutionary concept of photonic band gaps (PBGs) in periodic dielectric me-
28 dia, establishing the theoretical framework for electromagnetic wave manipula-
29 tion. This breakthrough catalyzed rapid theoretical and experimental advances:
30 Meade et al. [18] provided the first theoretical demonstration of two-dimensional
31 PBGs, while Villeneuve and Piché [19] analyzed band-gap formation in square
32 and hexagonal lattices. The consolidation of this progress culminated in the pa-
33 per by Joannopoulos [20], which demonstrated controlled electromagnetic wave

manipulation in photonic crystals with immediate practical impact.

Inspired by these photonic developments, the early 1990s witnessed the emergence of phononics as researchers began investigating analogous concepts for mechanical wave control in elastic media. Sigalas and Economou [21] provided the first definitive demonstration of elastic-wave band gaps in two-dimensional periodic systems in 1992, followed by Kushwaha et al. [22], who developed the foundational theoretical framework for acoustic band structures in periodic elastic composites. These pioneering contributions established the principles that would guide subsequent phononic crystal research [23].

Phononic crystals (PCs) emerged as artificial structures composed of periodic arrangements of materials with contrasting mechanical properties, typically involving inclusions embedded in a host matrix. This concept, formalized in the late 1990s by Laude and collaborators [24, 25], operates through Bragg scattering mechanisms that restrict wave propagation within specific frequency bands—termed band gaps—when the structural periodicity approaches half the wavelength [22, 23]. The theoretical foundation draws from classical works by Floquet [26], Bloch [27], and Brillouin [28], later consolidated through comprehensive reviews [29, 30].

Despite their effectiveness, PCs face a fundamental limitation for low-frequency applications: Bragg's condition $a = n\lambda/2$ necessitates large unit cells to attenuate low-frequency waves [30], challenging compact device design, particularly for flexural [31] or elastic waves in complex media [32]. However, locally resonant sonic crystals (LRSCs) overcome this limitation by utilizing internal resonances rather than pure Bragg scattering, enabling subwavelength operation where resonator-induced band gaps can occur even when $a \ll \lambda/2$. While Bragg effects may contribute to observed band gaps in this study, the primary mechanism is local resonance coupling, distinguishing our approach from traditional phononic crystals that rely exclusively on geometric periodicity.

The paradigm shift toward subwavelength metamaterials began with Liu et al.

[33] groundbreaking proposal of Locally Resonant Sonic Crystals (LRSCs). Unlike conventional PCs that rely on interference, LRSCs utilize internal resonances to form band gaps at subwavelength scales, enabling lattice constants two orders of magnitude smaller than the acoustic wavelength while achieving deep low-frequency attenuation in compact structures.

Subsequent research rapidly expanded and validated this concept across multiple domains. Wang et al. demonstrated subwavelength band gaps in 2D soft-inclusion composites [34] and extended the concept to 1D harmonic oscillator systems, revealing that stiffness contrast governs attenuation depth [35]. Hsu et al. [36] showed that Lamb wave band gaps in thin plates depend strongly on inclusion radius and thickness, while Oudich and colleagues explored waveguiding in curved and straight channels [37] and experimentally confirmed complete out-of-plane Lamb wave band gaps in stubbed plates using Brillouin spectroscopy and laser vibrometry [38].

The theoretical analysis of wave propagation in metamaterial plates has evolved through significant contributions to classical plate theory. The Kirchhoff–Love and Mindlin–Reissner theories—originally formulated by Kirchhoff [39], Love [40], Mindlin [41], and Reissner [42]—provide the foundation for understanding flexural wave propagation in thin and moderately thick plates. Advanced numerical methods, including the Plane Wave Expansion (PWE) approach [43] and its Extended version (EPWE) [44, 45], enable accurate band structure predictions in complex periodic systems.

Building upon these developments, Xiao et al. investigated flexural wave propagation in thin plates with periodic spring–mass resonators using EPWE [46], revealing the coexistence of Bragg-type and locally resonant gaps, as well as wide pseudo-gaps dependent on resonator natural frequency. Critically, their work demonstrated that the widest bandgap occurs when the directional resonance band gap and Bragg band gap are nearly coupled, and they provided an approximate initial design formula for achieving such optimal coupling con-

92 ditions. This coupling mechanism enables the formation of super-wide pseudo-
93 directional gaps through the combination of resonance and Bragg effects, with
94 the bandwidth being dramatically affected by the resonant frequency of local
95 resonators. Their subsequent work demonstrated that beam-like resonators pe-
96 riodically attached to plates can induce low-frequency complete band gaps for
97 flexural waves [47], with tunable resonator properties allowing significant control
98 over band gap location and width.

99 Recent advances have further refined our understanding of metamaterial plate
100 behavior. Miranda et al. analyzed multi-DOF resonator arrays using PWE
101 validated with finite element simulations (FEM) and experiments [48], reveal-
102 ing similar attenuation levels for square and triangular lattices, though square
103 configurations exhibited wider Bragg-type gaps. Their extension to thick plates
104 with spring–mass resonators, applying Mindlin–Reissner theory through com-
105 bined analytical, numerical, and experimental methods [49], confirmed simulta-
106 neous formation of locally resonant and Bragg-type band gaps, further validating
107 LRSCs as robust platforms for vibration attenuation.

108 The practical implementation of metamaterial concepts has yielded numerous
109 engineering applications. Flexural wave control in thin plates, demonstrated by
110 Lee and Ruzzene [50] and Yao et al. [51], has found significant relevance in
111 aerospace and automotive industries. Metamaterial barriers for vibration and
112 acoustic isolation have advanced through studies like Zouari et al. [52], while
113 acoustic panels for architectural acoustics were developed by Wang et al. [53].
114 The integration of multiple physical phenomena—including piezoelectric effects
115 for active control [54] and adaptive metamaterials with embedded shunt circuits
116 [55]—has opened new possibilities for smart, adaptive metamaterial systems.

117 Advanced design strategies have further enhanced metamaterial performance.
118 Fractal-based phononic structures, such as hierarchical porous designs by Lee
119 and Jeon [56], demonstrated that multi-level geometries can open multiple and
120 widened band gaps. Auxetic microstructured metamaterials have shown novel

121 wave-control mechanisms [57], while embedding multiple local resonators within
122 unit cells has proven effective [58]. Divergent-shaped unit cells, such as star-
123 shaped configurations [59], have demonstrated low-frequency, wide band-gap
124 behavior, with viscoelastic damping layers further broadening performance [58].

125 Recent investigations have explored the relationship between lattice geometry
126 and attenuation performance. Wang et al. [60] investigated sandwich plate
127 structures with periodically embedded plate-type resonators, demonstrating sig-
128nificant sound transmission loss, while Yan et al. [61] employed geometry op-
129timization to design diverse lattice configurations for enhanced low-frequency
130 vibration attenuation. The influence of resonator design on band-gap formation
131 has been extensively studied through impedance mismatch effects [62], modal
132 coupling influences, and multilayer resonator arrangements [63]. These studies
133 have revealed critical design parameters for attenuation performance.

134 Building upon these extensive developments, this study addresses the challenge
135 of low-frequency noise and vibration control by presenting the first systematic
136 comparative analysis of the elastic band structure of flexural waves in periodic
137 plates with five distinct lattice configurations. The research is motivated by
138 the critical need to quantify design trade-offs: while metamaterial solutions can
139 achieve 20-40 [dB] attenuation with only 5-15% mass penalties (compared to
140 150-300% for conventional approaches), empirical approaches to lattice design
141 prevent full optimization and economic gains.

142 The investigation examines single-degree-of-freedom (SDOF) local resonator sys-
143 tems (SR-SDOF) arranged in square, rectangular, and triangular lattices, as
144 well as multiple local resonator systems (MR-SDOF) in honeycomb and kagomé
145 lattices. These five geometries represent the fundamental design space for
146 2D lattice metamaterials: square and rectangular lattices establish the base-
147 line orthogonal configurations commonly employed in manufacturing; triangu-
148 lar lattices provide the highest symmetry achievable with single resonators per
149 unit cell; honeycomb configurations introduce the simplest dual-resonator ar-

150 chitecture with practical manufacturability; and kagomé lattices represent the
151 most complex three-resonator arrangement feasible within standard fabrica-
152 tion constraints. This selection encompasses the full spectrum from simple
153 (manufacturing-friendly) to complex (performance-optimized) configurations, en-
154 abling systematic evaluation of the geometry-performance-complexity trade-offs
155 critical for engineering implementation.

156 The comprehensive analysis employs both semi-analytical methods (PWE and
157 EPWE) and numerical simulations (FEM), demonstrating computational effi-
158 ciency improvements of two orders of magnitude while establishing quantitative
159 performance hierarchies among lattice configurations. This work provides crit-
160 ical insights into the dual influence of lattice geometry and resonator tuning,
161 enabling data-driven design decisions that can reduce development time by 60-
162 80% compared to trial-and-error approaches, while ensuring optimal solutions
163 for specific application requirements in weight-sensitive and performance-critical
164 engineering systems.

165 This paper is structured as follows: Section 2 presents the PWE approach for
166 periodic plates based on Kirchhoff-Love theory, detailing the mathematical for-
167 mulation for five lattice types (square, rectangular, triangular, honeycomb, and
168 kagomé) with spring-mass resonators, including the derivation of eigenvalue
169 problems and dispersion relations. Section 3 analyzes structure bands for 15 lo-
170 cal resonance frequency values ranging from 30 [Hz] to 200 [Hz], systematically
171 comparing band gap widths, attenuation depths, and frequency evolution across
172 all lattice configurations, while identifying critical performance metrics such as
173 the triangular lattice’s superior broadband performance and the kagomé’s ex-
174 ceptional low-frequency attenuation. Section 4 validates the semi-analytical
175 predictions through finite element simulations of 10×10 unit cell plates under
176 point force excitation, comparing receptance curves and transmission loss to
177 demonstrate the correlation between infinite-domain band structures and finite-
178 plate vibration attenuation. Conclusions are presented in Section 5, synthesiz-
179 ing the quantitative design guidelines and performance hierarchies discovered.

180 Appendix A and Appendix B provide the complete matrix formulations for
 181 PWE and EPWE implementations, including reciprocal lattice vectors, Fourier
 182 coefficients, and computational algorithms for complex wave vector extraction.
 183 Appendix C extends the analysis to metallic and composite materials (alu-
 184 minum and carbon/epoxy), demonstrating the universality of geometric perfor-
 185 mance principles across materials with $150\times$ stiffness variation. Appendix D
 186 presents a comprehensive framework for lattice selection in engineering appli-
 187 cations, providing quantitative decision tables and application-specific design
 188 guidelines derived from the comparative analysis.

189 **2. Formulating LRSC unit cell models**

190 This section presents a comprehensive formulation for thin LRSC plates using
 191 semi-analytical PWE and EPWE methods, based on Kirchhoff-Love plate theory
 192 [40].

193 *2.1. Theoretical foundations*

194 LRSC plates are modeled using Kirchhoff-Love theory for thin plates ($h/a < 0.1$)
 195 with spring-mass resonators providing local resonance effects (Figure 1).

196 This classical theory assumes plane sections remain plane and perpendicular
 197 to the neutral surface during bending, neglecting transverse shear deformation
 198 and rotatory inertia effects. The theory is valid when the plate thickness is
 199 much smaller than the characteristic wavelength, ensuring that flexural wave
 200 propagation is governed by the plate's bending stiffness rather than shear effects.
 201 The governing equation for flexural vibration with periodic resonator coupling
 202 is formulated in the frequency domain, as previously defined in works such as
 203 [46, 48]:

$$D\nabla^4 w(\mathbf{r}) - \omega^2 \rho h w(\mathbf{r}) = \sum_{j=1}^{N_j} \sum_{\mathbf{R}} p_j(\mathbf{r}_j + \mathbf{R}) \delta[\mathbf{r} - (\mathbf{r}_j + \mathbf{R})], \quad (1)$$

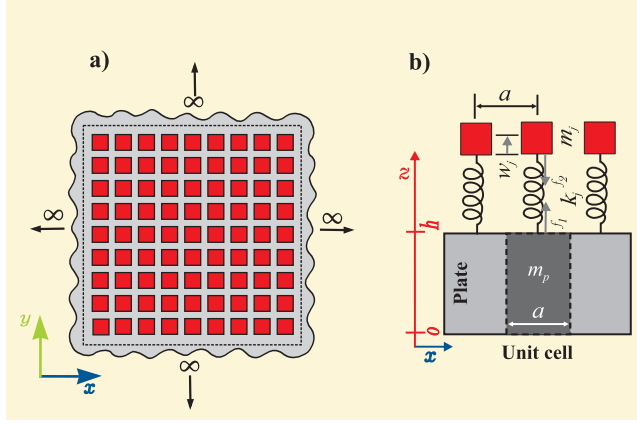


Figure 1: LRSC metamaterial configuration: (a) Infinite periodic array showing the global structure with spring-mass resonators (red squares) attached to the host plate. The dashed lines indicate the unit cell boundaries. (b) Detailed view of a single unit cell showing: plate mass m_p , resonator parameters (m_j , k_j , f_j), geometric dimensions (a , h), and coordinate system. The resonators provide local resonance at frequency $f_j = (2\pi^{-1})\sqrt{k_j/m_j}$.

where $D = E^*h^3/[12(1-\nu^2)]$ is the complex bending stiffness with $E^* = E(1 + i\eta_p)$ being the complex Young's modulus incorporating plate damping through loss factor η_p , \mathbf{R} are lattice vectors defining the periodic repetition of unit cells, \mathbf{r}_j are the positions of resonators within a unit cell, and N_j resonators per unit cell. Resonator-plate coupling follows:

$$p_j(\mathbf{r}_j + \mathbf{R}) = k_j^*[u_j(\mathbf{r}_j + \mathbf{R}) - w(\mathbf{r}_j + \mathbf{R})], \quad (2)$$

$$-\omega^2 m_j u_j(\mathbf{r}_j + \mathbf{R}) = -p_j(\mathbf{r}_j + \mathbf{R}), \quad (3)$$

where $u_j(\mathbf{r}_j + \mathbf{R})$ is the displacement of the j th resonator mass and $w(\mathbf{r}_j + \mathbf{R})$ is the flexural displacement of the plate at the resonator attachment point. The complex stiffness $k_j^* = k_j(1 + i\eta_j)$ incorporates the resonator damping effect.

Eliminating the resonator displacement u_j from Equations (2) and (3) yields the resonator coupling force:

$$p_j(\mathbf{r}_j + \mathbf{R}) = \frac{-k_j^*\omega^2}{\omega^2 - \omega_{j,0}^2(1 + i\eta_j)} w(\mathbf{r}_j + \mathbf{R}) \quad (4)$$

215 where $\omega_{j,0} = \sqrt{k_j/m_j}$ is the natural resonator frequency. Substituting this coupling into Equation (1) and applying periodic Floquet-Bloch conditions transforms the partial differential equation into a matrix eigenvalue problem via reciprocal space expansion, as detailed in the Appendix A.

219 The plane wave truncation parameter M in the expansion $(2M+1)^2$ determines
220 the computational accuracy of the PWE method. Based on established practices
221 for similar PC analyses [48, 49], this study employs $M = 3$ for single-resonator
222 and multi-resonator cases in the frequency range 10-200 [Hz] with lattice param-
223 eter $a = 0.10$ m, ensuring wavelength resolution $\lambda/a > 5$ for adequate spatial
224 discretization of the wave field.

225 *2.2. Semi-analytical methods overview*

226 This study employs two complementary semi-analytical approaches: Plane Wave
227 Expansion (PWE) and Extended Plane Wave Expansion (EPWE). Table 1 sum-
228 marizes their key characteristics and applications.

Table 1: Comparison between PWE and EPWE methods for LRSC plate analysis.

Aspect	PWE Method	EPWE Method
Wave vector \mathbf{k}	Real values only	$\mathbf{k} \in \mathbb{C}, \mathbf{k} = \Re(\mathbf{k}) + i\Im(\mathbf{k})$
Evanescence modes	Ignored	Naturally incorporated
Primary application	Band structure calculation $\omega(\mathbf{k})$	Unit cell attenuation $\mathbf{k}(\omega)$
Brillouin zone	Restricted to first zone	No restriction
Bandgap analysis	Identifies frequency ranges	Quantifies unit cell attenuation
Computational cost	Lower (eigenvalue problem)	Higher (generalized eigenvalue)
Physical insight	Propagating wave modes	Evanescence wave modes decay in bandgaps

²²⁹ The combination of both methods provides complete bandgap characterization.

²³⁰ PWE solves the forward eigenvalue problem:

$$[\mathbf{K} - \omega^2 \mathbf{M}] \boldsymbol{\phi} = 0, \quad \omega = \omega(\mathbf{k}) \quad (5)$$

²³¹ while EPWE solves the inverse problem for complex wave vectors:

$$[\mathbf{A}_3 k^3 + \mathbf{A}_2 k^2 + \mathbf{A}_1 k + \mathbf{A}_0] \boldsymbol{\psi} = 0, \quad k = k(\omega) \quad (6)$$

²³² The unit cell attenuation constant is defined as $\mu = \Im k$. With these analytical
²³³ tools established, the following section examines how different lattice geometries
²³⁴ influence the band structure formation and attenuation characteristics, while the
²³⁵ corresponding matrix formulation can be found in Appendix B.

²³⁶ *2.3. Periodic lattice configurations*

²³⁷ Five lattice geometries with varying resonator configurations are analyzed: square
²³⁸ (1 resonator), rectangular (1), triangular (1), honeycomb (2), and kagomé (3).

²³⁹ These geometries span orthogonal to complex lattice symmetries, enabling com-
²⁴⁰ prehensive bandgap performance evaluation.

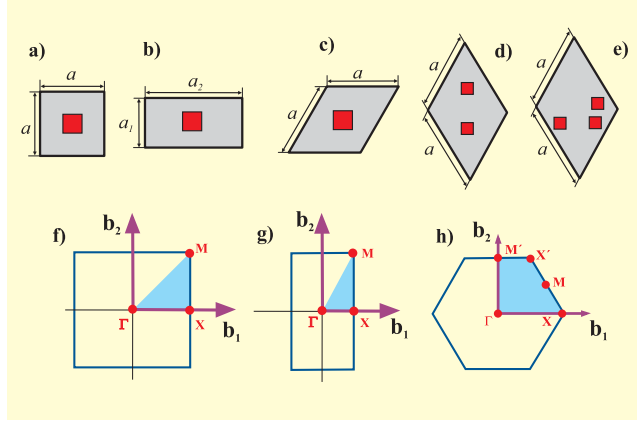


Figure 2: LRSC unit cells and FIBZ paths: (a) square, (b) rectangular, (c) triangular, (d) honeycomb, (e) kagomé lattices. Red squares: resonators. FIBZ high-symmetry paths: (f) Square, (g) Rectangular and (h) Triangular/Honeycomb/Kagomé.

²⁴¹ Primitive lattice vectors are: $\mathbf{a}_{1,2} = a\mathbf{e}_{1,2}$ (square), $\mathbf{a}_{1,2} = a_{x,y}\mathbf{e}_{1,2}$ (rectangular),
²⁴² $\mathbf{a}_1 = a\mathbf{e}_1$ and $\mathbf{a}_2 = a(-\frac{1}{2}\mathbf{e}_1 + \frac{\sqrt{3}}{2}\mathbf{e}_2)$ (triangular), $\mathbf{a}_{1,2} = a\mathbf{e}_{1,2}$ (honeycomb), and
²⁴³ $\mathbf{a}_1 = a\sqrt{3}(\mathbf{e}_1 - \frac{1}{\sqrt{3}}\mathbf{e}_2)$ and $\mathbf{a}_2 = a\sqrt{3}(\mathbf{e}_1 + \frac{1}{\sqrt{3}}\mathbf{e}_2)$ (kagomé). Reciprocal lattice
²⁴⁴ vectors follow standard crystallographic relations $\mathbf{b}_i = 2\pi(\mathbf{a}_j \times \mathbf{e}_z)/(\mathbf{a}_i \cdot (\mathbf{a}_j \times \mathbf{e}_z))$.

²⁴⁵ 2.4. PWE for thin LRSC unit cell thin plate configurations

²⁴⁶ PWE transforms the governing PDE into a matrix eigenvalue problem via
²⁴⁷ Fourier expansion in reciprocal space. The displacement field follows Floquet-
²⁴⁸ Bloch theorem:

$$w(\mathbf{r}) = e^{i\mathbf{k}\cdot\mathbf{r}} \sum_{\mathbf{G}} w(\mathbf{G}) e^{i\mathbf{G}\cdot\mathbf{r}} = \sum_{\mathbf{G}} w(\mathbf{G}) e^{i(\mathbf{k}+\mathbf{G})\cdot\mathbf{r}} \quad (7)$$

²⁴⁹ where reciprocal lattice vectors $\mathbf{G} = m\mathbf{b}_1 + n\mathbf{b}_2$ with integers $(m, n) \in [-M, M]$
²⁵⁰ and basis vectors $\mathbf{b}_i = (2\pi/S)(\mathbf{a}_j \times \mathbf{e}_z)$ for unit cell area S , consistent with the
²⁵¹ $(2M+1)^2$ plane wave truncation used in computational implementation.

252 Resonator displacements satisfy:

$$w(\mathbf{r}_j) = \sum_{\mathbf{G}} w(\mathbf{G}) e^{i(\mathbf{k} + \mathbf{G}) \cdot \mathbf{r}_j} \quad (8)$$

253 The eigenvalue problem formulation yields:

$$[\mathbf{K} - \omega^2 \mathbf{M}] \{ \mathbf{q} \} = \mathbf{0} \quad (9)$$

254 where \mathbf{K} and \mathbf{M} are stiffness and mass matrices, and $\mathbf{q} = [\mathbf{w}^T, \mathbf{u}^T]^T$ contains
255 both plate wave amplitudes $\mathbf{w} = [w(\mathbf{G}_1), \dots, w(\mathbf{G}_{N_g})]^T$ and resonator displace-
256 ments $\mathbf{u} = [u_1, \dots, u_{N_j}]^T$. Matrix dimension is $[(2M+1)^2 + N_j] \times [(2M+1)^2 + N_j]$
257 with $N_g = (2M + 1)^2$ plane waves and N_j resonators per unit cell. Complete
258 matrix assembly algorithms are detailed in Appendix A.

259 The stiffness matrix \mathbf{K} from PWE contains fourth-order plate operators $|\mathbf{k} + \mathbf{G}|^4$
260 and resonator coupling terms that become frequency-dependent in EPWE. The
261 mass matrix \mathbf{M} contributions transform to complex dynamic stiffness expres-
262 sions $D_j(\omega)$ in the inverse formulation. This matrix relationship enables consis-
263 tent implementation of both forward $\omega(\mathbf{k})$ and inverse $\mathbf{k}(\omega)$ problems using the
264 same physical parameters and geometric definitions.

265 2.5. EPWE for thin LRSC unit cell thin plate configurations

266 EPWE reformulates the eigenvalue problem to solve for complex wave vectors
267 $\mathbf{k}(\omega)$ at prescribed frequencies, enabling direct analysis of evanescent modes
268 and wave attenuation within bandgaps. The displacement field maintains the
269 Floquet-Bloch form:

$$w(\mathbf{r}) = e^{i\mathbf{k} \cdot \mathbf{r}} \sum_{\mathbf{G}} w(\mathbf{G}) e^{i\mathbf{G} \cdot \mathbf{r}}, \quad \mathbf{k} = k_r + ik_i \quad (10)$$

270 where the complex wave vector $\mathbf{k} \in \mathbb{C}$ allows for exponentially decaying modes
271 with attenuation constant k_i .

272 Resonator displacements follow the same expansion as Equation (8). Substitu-
273 tion into the governing equation yields a polynomial eigenvalue problem:

$$[\mathbf{A}_3 k^3 + \mathbf{A}_2 k^2 + \mathbf{A}_1 k + \mathbf{A}_0] \psi = 0 \quad (11)$$

274 where coefficient matrices \mathbf{A}_i contain lattice geometry and resonator coupling
275 terms. The resonator dynamic stiffness incorporates frequency-dependent ef-
276 fects:

$$D_j(\omega) = k_j^* - \frac{(k_j^*)^2}{k_j^* - \omega^2 m_j} \quad (12)$$

277 Solution via companion matrix linearization provides complex eigenvalues $k =$
278 $k_r + ik_i$, where $\Im\{k\}$ quantifies evanescent decay. The unit cell attenuation
279 constant $\mu = \Im\{k\}$ directly measures wave attenuation within bandgaps. The
280 polynomial eigenvalue problem is solved by transforming Eq. (11) into a gener-
281 alized linear eigenvalue problem of size $4N_g \times 4N_g$, where eigenvector tracking
282 ensures mode continuity across frequency. Complete matrix formulations and
283 computational algorithms are provided in Appendix B.

284 The proposed semi-analytical methods (PWE and EPWE($\Re(\mathbf{k})$)) are validated
285 using finite element method (FEM) simulations in COMSOL Multiphysics 5.6
286 with quadratic shell elements and Floquet periodic boundary conditions. The
287 following section presents comprehensive computational efficiency and accuracy
288 comparisons between PWE/EPWE and FEM through detailed simulated exam-
289 ples.

290 The semi-analytical formulation is valid under the following constraints: (i)
291 thin plate approximation: $h/a < 0.1$ ensuring flexural wave dominance over
292 shear effects; (ii) small amplitude assumption: linear elastic response with plate
293 displacements $w \ll h$; (iii) frequency limitations: $\omega < \omega_c = 0.5\sqrt{D/(\rho h a^4)}$ to
294 remain within the fundamental dispersion branch; (iv) weak coupling regime:
295 resonator mass ratio $m_j/(m_p S) < 0.2$ ensuring perturbative coupling validity.
296 These constraints ensure that the Kirchhoff-Love theory assumptions remain
297 physically meaningful and that the plane wave expansion converges within the
298 specified truncation limits.

299 The comprehensive mathematical framework established in this section provides
300 the theoretical foundation for systematic lattice comparison. The PWE method

enables efficient computation of dispersion relations $\omega(\mathbf{k})$ for identifying band gap formation, while EPWE quantifies attenuation coefficients $k(\omega)$ within these gaps. The convergence criteria and validity constraints ensure reliable predictions across the target frequency range (10-200 [Hz]) for all five geometric configurations. The results obtained using this EPWE formulation will be examined in detail in Section 4 for the finite plate model. With this robust analytical foundation established, the following section validates these theoretical predictions through systematic numerical analysis, demonstrating the practical applicability of the framework for engineering design and establishing clear performance hierarchies among the investigated lattice geometries.

3. Simulated Examples and Validation

This section validates theoretical predictions through systematic analysis of five lattice configurations: single-resonator (square, rectangular and triangular) and multi-resonator systems (honeycomb and kagomé). The investigation establishes quantitative performance hierarchies and demonstrates PWE-FEM correlation using physically realizable parameters optimized for low-frequency applications (10-200 [Hz]) with 3D printable Vero White Plus polymer [48]. While this section focuses on polymeric material for experimental validation feasibility, Appendix C extends the analysis to structural materials (aluminum alloy [46] and carbon/epoxy composite [64]), demonstrating the universality of geometric performance principles across materials with $150\times$ stiffness variation.

The material and geometric parameters in Table 2 enable systematic performance evaluation while maintaining manufacturing constraints:

Table 2: Elastic metamaterial thin plate geometry and material properties with justifications.

Parameter	Value	Justification
Mass density ρ	600 kg/m ³	Representative polymer density (PLA, ABS) for rapid prototyping
Young's modulus E^*	0.86 GPa	Measured for Vero White Plus. Complex form $E^* = E(1 + i\eta_p)$ for viscoelasticity
Loss factor η_p	0.01	Representative polymer damping at room temperature
Poisson's ratio ν	0.36	Standard polymer value
Plate thickness h	0.002 m	Ensures thin plate validity ($h/a = 0.02 \ll 0.1$) and manufacturability
Lattice parameter a	0.10 m	Optimized for 10-200 Hz: enables sub-wavelength resonance
Mass ratio γ	0.5	Maximizes band gap width (50% of plate mass per unit cell)
Resonator loss η_j	0.01	Matched to plate damping
Resonator stiffness	Complex	$k_j^* = (4\gamma\rho Sh\pi^2 f_j^2)/(1 + i\eta_j)$ [N/m] with damping

324 Using these material parameters, the geometric and physical properties for
 325 each lattice configuration are calculated as shown in Table 3, where the lat-
 326 tice parameter a is kept constant to enable direct performance comparison.
 327 This constant-parameter approach isolates geometric influences from frequency-
 328 scaling effects, providing objective performance hierarchy based on intrinsic
 329 properties—essential for engineering applications where devices must fit prede-
 330 termined spatial constraints (e.g., aerospace, automotive). Additionally, main-
 331 taining constant a enables meaningful relative bandwidth analysis (η_{rel}), where
 332 normalization by center frequency removes scaling effects and reveals intrinsic
 333 geometric efficiency. Theoretically, this maintains Bloch-Floquet consistency:
 334 varying lattice constant creates different Brillouin zones ($\propto 2\pi/a$), complicating
 335 direct comparison of dispersion relations. This follows established practice in

³³⁶ phononic/photonic research [19, 46, 61].

Table 3: Geometric and physical properties of five LRSC lattice configurations. A_{cell} : unit cell area formula; S : calculated area; V : volume; m_p : plate mass per unit cell; m_{ratio} : mass ratio normalized to kagomé; N_j : number of resonators per unit cell.

Lattice	A_{cell}	$S[\text{m}^2]$	$V[\text{m}^3]$	$m_p [\text{kg}]$	m_{ratio}	N_j
Kagomé	$2a^2\sqrt{3}$	3.46e-02	6.93e-05	4.16e-02	1.00	3
Honeycomb	$\frac{3a^2\sqrt{3}}{2}$	2.60e-02	5.20e-05	3.12e-02	0.75	2
Square	a^2	1.00e-02	2.00e-05	1.20e-02	0.29	1
Triangular	$\frac{a^2\sqrt{3}}{2}$	0.87e-02	1.73e-05	1.04e-02	0.25	1
Rectangular	$a_1 \times a_2$	0.50e-02	1.00e-05	0.60e-02	0.14	1

³³⁷ The mass ratio is defined as:

$$m_{ratio} = \frac{m_{p,i}}{m_{p,\text{kagomé}}} = \frac{m_{p,i}}{4.16 \times 10^{-2}}, \quad (13)$$

³³⁸ where $m_{p,i}$ is the plate mass per unit cell for lattice configuration i , and $m_{p,\text{kagomé}} =$
³³⁹ 4.16×10^{-2} kg represents the reference mass (kagomé lattice with largest unit cell
³⁴⁰ area). This normalization enables direct material efficiency comparison across
³⁴¹ different lattice geometries. This normalization reveals material efficiency differ-
³⁴² ences: triangular (25%) and rectangular (14%) lattices achieve superior perfor-
³⁴³ mance with minimal material usage compared to kagomé. The computational
³⁴⁴ implementation employs optimized discretization parameters in Table 4 to bal-
³⁴⁵ ance numerical accuracy with efficiency.

Table 4: Parameters of mesh discretization in FEM (a/n), plane wave truncation in PWE (M), and processing times for the five studied lattice configurations.

Lattice	n	$a/n [\text{m}]$	M	$t_{\text{FEM}} [\text{s}]$	$t_{\text{PWE}} [\text{s}]$
Square	20	5.00×10^{-3}	3	9.08×10^2	4.30×10^{-1}
Rectangular	20	5.00×10^{-3}	3	6.22×10^2	4.20×10^{-1}
Triangular	20	5.00×10^{-3}	3	14.48×10^2	7.30×10^{-1}
Honeycomb	22	4.50×10^{-3}	3	35.22×10^2	8.20×10^{-1}
Kagomé	24	4.50×10^{-3}	3	50.54×10^2	8.90×10^{-1}

346 The discretization parameters (n for mesh density, M for plane-wave truncation)
 347 and the corresponding computational times illustrate the efficiency of the
 348 PWE method compared with FEM. All numerical simulations were performed
 349 in COMSOL Multiphysics (v5.6) and MATLAB (R2021a) on an AMD Ryzen 5
 350 3600 workstation (6 cores, 12 threads, 3.6 GHz, 16 GB DDR4 RAM, Windows
 351 10).

352 Systematic comparison between PWE and FEM predictions validates the semi-
 353 analytical framework accuracy. Table 5 presents quantitative validation metrics
 354 for characteristic frequencies across all lattice configurations.

Table 5: PWE-FEM validation: frequency comparison at key points in FIBZ with error metrics.^a

Lattice	Point	f_{PWE} [Hz]	f_{FEM} [Hz]	Error [%]	RMSE
Square	Γ	42.16	42.48	0.75	
	X	85.32	84.91	0.48	1.24
	M	118.74	117.82	0.78	
Rectangular	Γ	38.92	39.15	0.59	
	X	79.48	78.94	0.68	1.18
	M	112.36	111.54	0.73	
Triangular	Γ	45.83	46.02	0.41	
	X	91.67	91.24	0.47	0.89
	M	127.45	126.78	0.53	
Honeycomb	Γ	31.24	31.46	0.70	
	X	62.48	62.91	0.68	1.42
	M	98.73	99.58	0.85	
Kagomé	Γ	21.37	21.52	0.70	
	X	42.74	43.18	1.02	1.67
	M	68.19	69.04	1.24	
Overall Statistics:				0.68 ± 0.24	1.28

355 PWE-FEM validation shows excellent agreement: $0.68\% \pm 0.24\%$ error with
 356 $1800\text{-}5700\times$ computational speedup, confirming accuracy and efficiency for all

³⁵⁷ lattice configurations. For hexagonal lattices (triangular, honeycomb, kagomé),
³⁵⁸ only primary symmetry points (Γ , X , M) are validated as they fully define
³⁵⁹ the irreducible Brillouin zone; additional points (X' , M') are equivalent due to
³⁶⁰ 6-fold symmetry.

³⁶¹ *3.1. Band structures for square, rectangular and triangular SR-SDOF lattices*

³⁶² This subsection analyzes single-resonator lattices with distinct symmetry classes:
³⁶³ square (4-fold), rectangular (anisotropic), and triangular (6-fold). Starting with
³⁶⁴ square lattice analysis, Figure 3 establishes the square lattice as the baseline
³⁶⁵ configuration for single-resonator metamaterials, demonstrating excellent PWE-
³⁶⁶ FEM agreement across the entire frequency spectrum. Resonator stiffness values
³⁶⁷ are calibrated to achieve $f_j = 80$ Hz for direct geometric comparison.

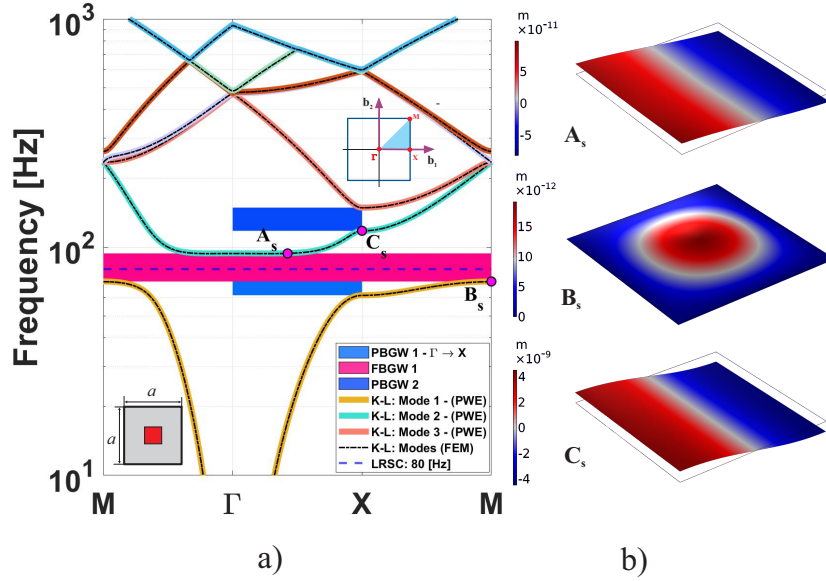


Figure 3: (a) Band structure computed with PWE and FEM for a square lattice unit cell with a single resonator with $f_r = 80$ [Hz] in a thin plate. FBGW 1 - $f_1 = 70.72$ [Hz], $f_2 = 93.88$ [Hz], $\Delta f_{12} = 23.16$ [Hz], PBGW 1 - $f_1 = 61.54$ [Hz], $f_2 = 93.88$ [Hz], $\Delta f_{12} = 32.33$ [Hz], PBGW 2 - $f_1 = 117.91$ [Hz], $f_2 = 149$ [Hz], $\Delta f_{12} = 31.09$ [Hz]. (b) Waves mode shapes for a square lattice unit cell with a single resonator in a different points of edges in a real band structure computed by FEM: Point A_s ($k = 1.42$ [m^{-1}], $f = 93.87$ [Hz]), Point B_s ($k = 3.00$ [m^{-1}], $f = 70.55$ [Hz]), Point C_s ($k = 2.00$ [m^{-1}], $f = 117.82$ [Hz]).

368 Dispersion analysis reveals local resonance creating FBGW 1 ($\Delta f_{12} = 23.16$
 369 [Hz], $f_1 = 70.72$ [Hz], $f_2 = 93.88$ [Hz]) with resonator frequency $f_j = 80$ [Hz]
 370 strategically positioned between edge wave modes for optimal energy extraction.
 371 Mode shapes (Figure 3b) show anti-resonance at point B_s , where the resonator
 372 creates destructive interference trapping wave energy and preventing propagation.
 373

374 Square lattice analysis reveals FBGW 1 ($\Delta f_{12} = 23.16$ [Hz]) and directional
 375 PBGWs, demonstrating resonator-plate hybridization through avoided crossings.
 376 Bragg scattering contributes additional wave interference at specific crystallo-
 377 graphic points.

378 Parametric analysis (Figure 4) investigates 15 resonator frequencies: panels (a-

379 c) show representative cases ($f_j = 10, 105, 150$ [Hz]), panels (d-e) track edge
 380 frequency evolution (f_1, f_2), and panel (f) reveals FBGW 1 bandwidth optimi-
 381 zation:

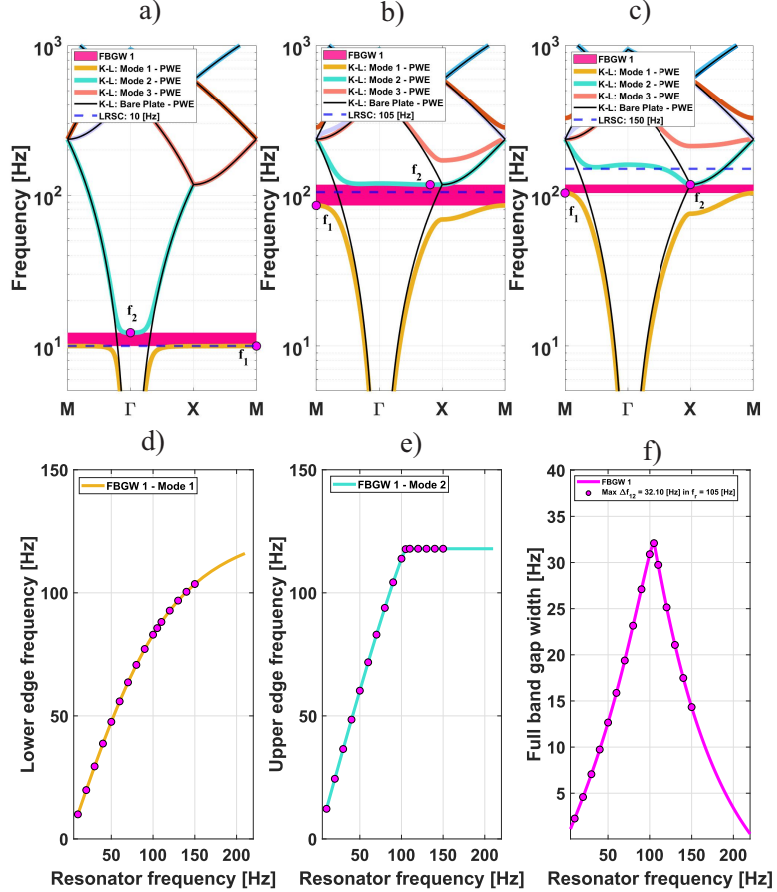


Figure 4: Results using in PWE for square lattice (a) LRSC in $f_j = 10$ [Hz], (b) LRSC in $f_j = 105$ [Hz] and (c) LRSC in $f_j = 150$ [Hz]. (d) f_1 - Lower edge frequencies of the first band mode as a function of local resonance. (e) f_2 - Upper edge frequencies of the second band mode as a function of local resonance. (f) FBGW 1 as function of resonator frequency.

382 Parametric analysis reveals three regimes: mass-loading ($f_j = 10$ [Hz], $\Delta f_{12} =$
 383 2.26 [Hz]), optimal coupling ($f_j = 105$ [Hz], $\Delta f_{12} = 32.10$ [Hz]), and stiffness-
 384 dominated ($f_j = 150$ [Hz], $\Delta f_{12} = 14.33$ [Hz]). This resonator frequency tun-
 385 ing behavior demonstrates that systematic variation of f_j enables controlled

³⁸⁶ bandgap engineering.

³⁸⁷ Edge frequency evolution reveals asymmetric band gap formation: f_1 increases
³⁸⁸ linearly with f_j (direct resonator control), while f_2 saturates at Bragg limit
³⁸⁹ $f_B = 117.91$ [Hz]—an intrinsic geometric ceiling independent of resonator tun-
³⁹⁰ ing. This Bragg frequency is calculated using the analytical formula derived
³⁹¹ by Xiao et al. [46] for square lattice configurations: $f_B = (1/2\pi)(\pi/a)^2\sqrt{D/\rho h}$,
³⁹² where the Γ -X direction ($\phi = 0$) provides the limiting frequency for the second
³⁹³ mode. Maximum bandwidth $\Delta f_{12} = 32.10$ [Hz] at $f_j = 105$ [Hz] represents op-
³⁹⁴ timal balance between local resonance (controlling f_1) and geometric dispersion
³⁹⁵ (limiting f_2), with subsequent decay reflecting saturation as f_2 approaches f_B .

³⁹⁶ The peak position at $f_j = 105$ [Hz] $\approx 0.89f_B$ reveals a universal design rule
³⁹⁷ for locally resonant metamaterials: optimal performance occurs when the res-
³⁹⁸ onator frequency is positioned slightly below the Bragg frequency, maximizing
³⁹⁹ the interaction between local and geometric scattering mechanisms. This con-
⁴⁰⁰ firms the fundamental importance of resonator frequency tuning for achieving
⁴⁰¹ optimal bandgap performance.

⁴⁰² Next, rectangular lattice analysis, the transition from square to rectangular ge-
⁴⁰³ ometry introduces geometric anisotropy that fundamentally alters metamaterial
⁴⁰⁴ behavior through two primary mechanisms: reduced unit cell area (0.50×10^{-2}
⁴⁰⁵ m^2 vs. $1.00 \times 10^{-2} m^2$ for square) and directional wave propagation asymmetry.

⁴⁰⁶ Figure 5 quantifies these geometric effects on band gap formation:

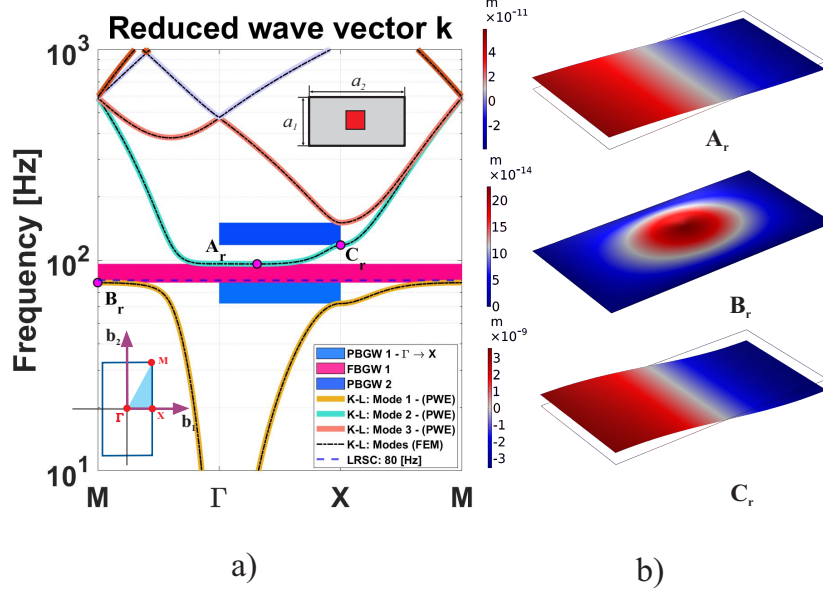


Figure 5: (a) Band structure computed with PWE and FEM for a rectangular lattice unit cell with a single resonator with $f_r = 80$ [Hz] in a thin plate. FBGW 1 - $f_1 = 78.23$ [Hz], $f_2 = 95.97$ [Hz], $\Delta f_{12} = 17.74$ [Hz], PBGW 1 - $f_1 = 62.27$ [Hz], $f_2 = 95.97$ [Hz], $\Delta f_{12} = 33.70$ [Hz], PBGW 2 - $f_1 = 117.91$ [Hz], $f_2 = 150.66$ [Hz], $\Delta f_{12} = 32.64$ [Hz]. (b) Wave mode shapes for a rectangular lattice unit cell with a single resonator in a different points of edges in a real band structure computed by FEM: Point A_r ($k = 1.31$ [m^{-1}], $f = 95.97$ [Hz]), Point B_r ($k = 0$ [m^{-1}], $f = 78.23$ [Hz]), Point C_r ($k = 2.00$ [m^{-1}], $f = 117.84$ [Hz]).

407 Rectangular lattice shows reduced FBGW 1 ($\Delta f_{12} = 17.74$ [Hz]) due to 50%
 408 smaller unit cell area, with optimal frequency shifted to $f_j = 99$ Hz. Maximum
 409 bandwidth $\Delta f_{12} = 20.53$ [Hz] represents 36% penalty versus square lattice,
 410 confirming unit cell area governs resonator effectiveness.

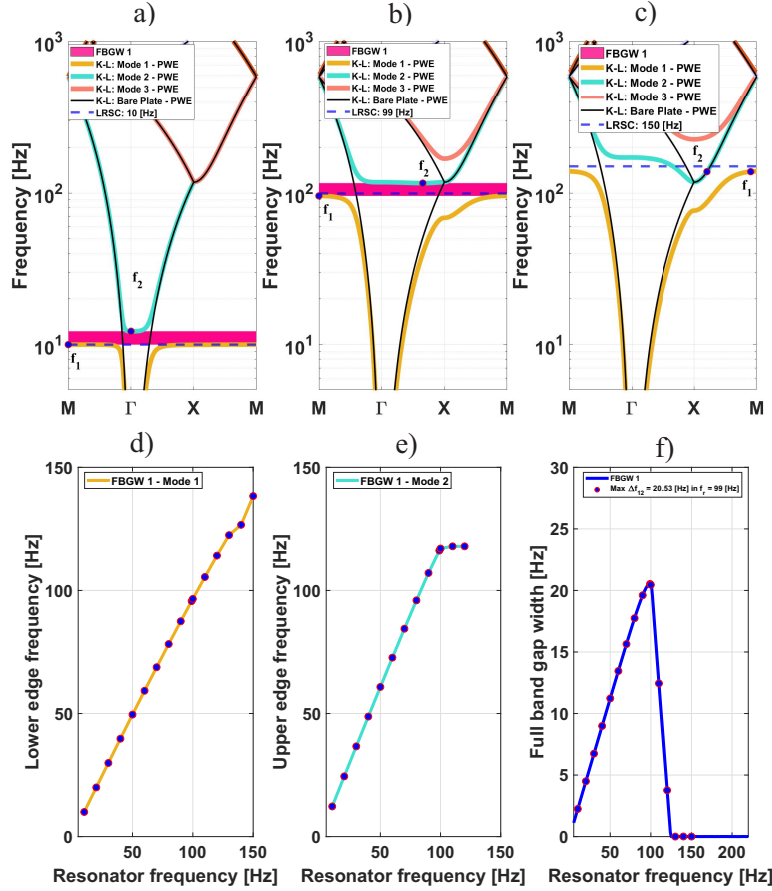


Figure 6: Results in PWE for rectangular lattice (a) LRSC in $f_j = 10$ [Hz], (b) LRSC in $f_j = 99$ [Hz] and (c) LRSC in $f_j = 150$ [Hz]. (d) f_1 - Lower edge frequencies of the first band mode as a function of local resonance. (e) f_2 - Upper edge frequencies of the second band mode as a function of local resonance. (f) FBGW 1 as function of resonator frequency.

411 Parametric analysis (Figure 6) reveals geometric constraints: premature band-
 412 width maximum at $f_j = 99$ [Hz] (36% penalty vs. square), complete band gap
 413 disappearance at $f_j = 150$ [Hz] (fundamental frequency cutoff), and compressed
 414 operational range with rapid decay beyond $f_j = 120$ [Hz]. Aspect ratio creates
 415 anisotropic resonator-plate coupling—reduced a_2 direction area weakens flexural
 416 mode interaction, producing directionality-dependent scattering and establishing
 417 geometric aspect ratio as a critical design parameter.

418 Triangular lattice provides six-fold symmetry despite 13% smaller unit cell area,
 419 achieving superior performance through multiple equivalent wave scattering
 420 pathways.

421 Figure 7 demonstrates the geometric advantage of triangular packing:

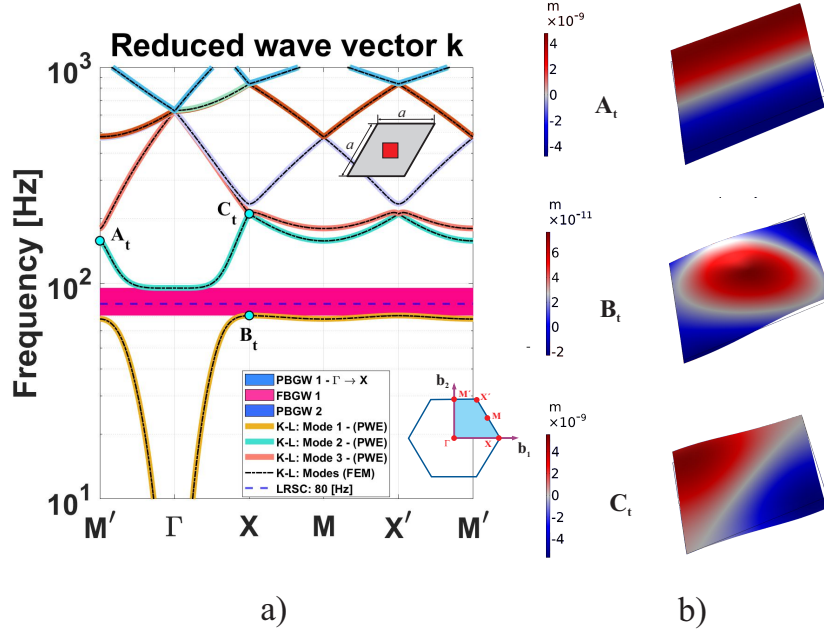


Figure 7: (a) Band structure computed with PWE and FEM for a triangular lattice unit cell with a single resonator with $f_r = 80$ [Hz] in a thin plate. FBGW 1 - $f_1 = 70.84$ [Hz], $f_2 = 95.08$ [Hz], $\Delta f_{12} = 24.24$ [Hz]. (b) Wave mode shapes for a triangular lattice unit cell with a single resonator in different points of edges in a real band structure computed by FEM: Point A_t ($k = 0$ [m^{-1}], $f = 157.05$ [Hz]), Point B_t ($k = 2.00$ [m^{-1}], $f = 70.71$ [Hz]), Point C_t ($k = 2.00$ [m^{-1}], $f = 209.99$ [Hz]).

422 Triangular lattice achieves FBGW 1 ($\Delta f_{12} = 24.24$ [Hz]) without partial band
 423 gaps, demonstrating isotropic wave blocking. Maximum bandwidth $\Delta f_{12} =$
 424 55.40 [Hz] at $f_j = 145$ [Hz] represents 73% improvement over square lattice,
 425 confirming geometric superiority. The triangular lattice parametric analysis
 426 reveals breakthrough performance that establishes this geometry as the optimal
 427 single-resonator metamaterial architecture. Figure 8a) ($f_j = 10$ [Hz]) shows

428 typical low-frequency behavior, while Figure 8b) ($f_j = 145$ [Hz]) captures the
 429 remarkable peak performance where the triangular lattice achieves its maximum
 430 bandwidth.

431 Figure 8c) ($f_j = 150$ [Hz]) demonstrates the exceptional bandwidth stability
 432 that distinguishes the triangular lattice from square and rectangular configura-
 433 tions. The edge frequency evolution in Figures 8d-e) reveals the underlying
 434 mechanisms responsible for superior performance.

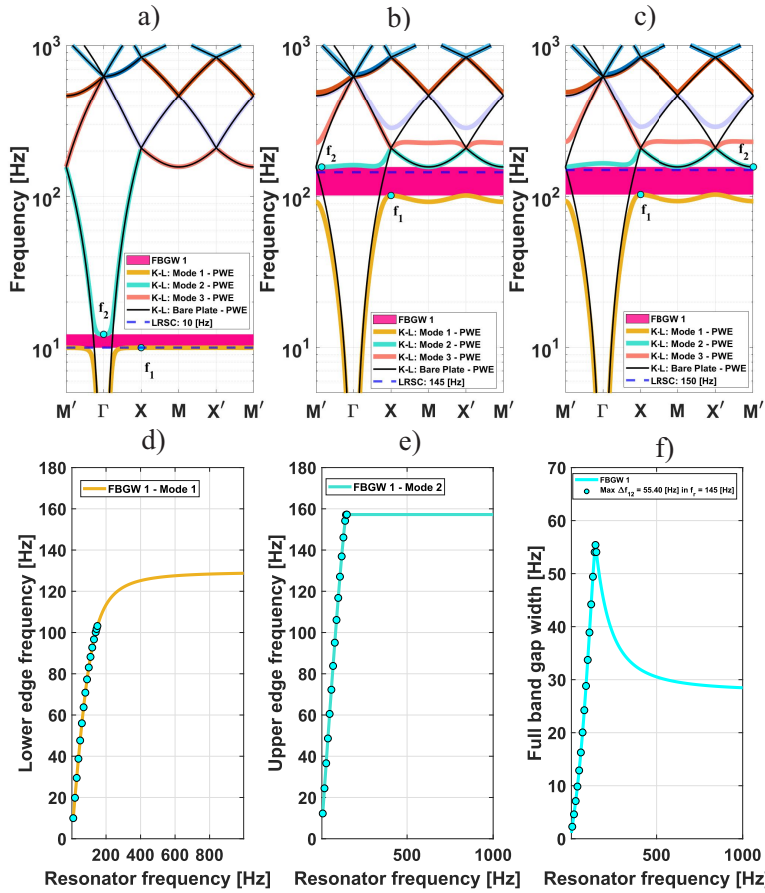


Figure 8: Results in PWE for triangular lattice (a) LRSC in $f_j = 10$ [Hz], (b) LRSC in $f_j = 99$ [Hz] and (c) LRSC in $f_j = 150$ [Hz]. (d) f_1 - Lower edge frequencies of the first band mode as a function of local resonance. (e) f_2 - Upper edge frequencies of the second band mode as a function of local resonance. (f) FBGW 1 as function of resonator frequency.

435 Figure 8b) documents a breakthrough in metamaterial performance with max-
436 imum bandwidth $\Delta f_{12} = 55.40$ [Hz] at $f_j = 145$ [Hz] – representing a 73%
437 improvement over the square lattice baseline and a 170% improvement over
438 the rectangular configuration. This exceptional performance occurs at a signifi-
439 cantly higher optimal frequency ($f_j = 145$ [Hz] vs. 105 [Hz] for square), indicat-
440 ing that the triangular geometry extends the operational frequency range while
441 simultaneously enhancing peak performance. The demonstrated tuning capabil-
442 ity across the full frequency spectrum extends the foundational work of Xiao et
443 al. [46] on resonator frequency optimization, revealing that geometric symmetry
444 fundamentally alters the achievable bandwidth-frequency relationship.

445 Exceptional bandwidth stability (Figure 8f): unlike square/rectangular lattices
446 with rapid decay, triangular maintains bandwidth >20 Hz across extended fre-
447 quency ranges through six-fold rotational symmetry providing multiple equiva-
448 lent scattering pathways. This creates robust wave-resonator coupling less sen-
449 sitive to frequency detuning, demonstrating that lattice symmetry dominates
450 over unit cell area—despite smaller area than square, superior symmetry en-
451 ables area-normalized efficiency exceeding simple area scaling.

452 Single-resonator lattice synthesis: The comprehensive analysis of SR-SDOF lat-
453 tices reveals fundamental design principles governing metamaterial optimization:
454 1. Geometric symmetry dominates over unit cell area (triangular $>$ square $>$
455 rectangular performance) 2. Optimal frequency scaling follows the universal
456 relationship $f_{j,opt} \approx 0.89f_B$ across all geometries, consistent with the resonance-
457 Bragg coupling principle established by Xiao et al. [46], where optimal band-
458 width emerges from strategic positioning of resonator frequencies relative to
459 geometric dispersion limits 3. Bandwidth robustness correlates directly with ro-
460 tational symmetry order (6-fold $>$ 4-fold $>$ 2-fold) 4. Area-normalized efficiency
461 reaches maximum in triangular configurations through isotropic wave coupling.
462 These findings establish the physical foundation for advancing to multi-resonator
463 architectures, where resonator coupling introduces new phenomena beyond sim-
464 ple scaling effects.

465 *3.2. Band structures calculation for honeycomb and kagomé MR-SDOF lattices*

466 This subsection explores multi-resonator metamaterial architectures that in-
467 troduce resonator coupling mechanisms fundamentally different from single-
468 resonator systems. The transition from SR-SDOF to MR-SDOF creates coupled
469 oscillator networks within each unit cell, generating multiple band gaps through
470 distinct physical mechanisms.

471 Honeycomb dual-resonator geometry positions two identical resonators at $\mathbf{r}_1 =$
472 $a(0, 1/2)$ and $\mathbf{r}_2 = -a(0, 1/2)$, creating symmetric coupling enabling both in-
473 phase and anti-phase oscillation modes. Unlike single-resonator systems with
474 independent plate interaction, dual-resonator systems exhibit collective behav-
475 ior (cooperative/competitive oscillations) creating distinct eigenfrequencies that
476 generate multiple band gaps. Increased stiffness $k_j = 1969$ [N/m] maintains tar-
477 get frequency $f_j = 80$ [Hz] accounting for reduced effective mass per resonator.

478 Figure 9 demonstrates the revolutionary advance achieved through multi-resonator
479 coupling:

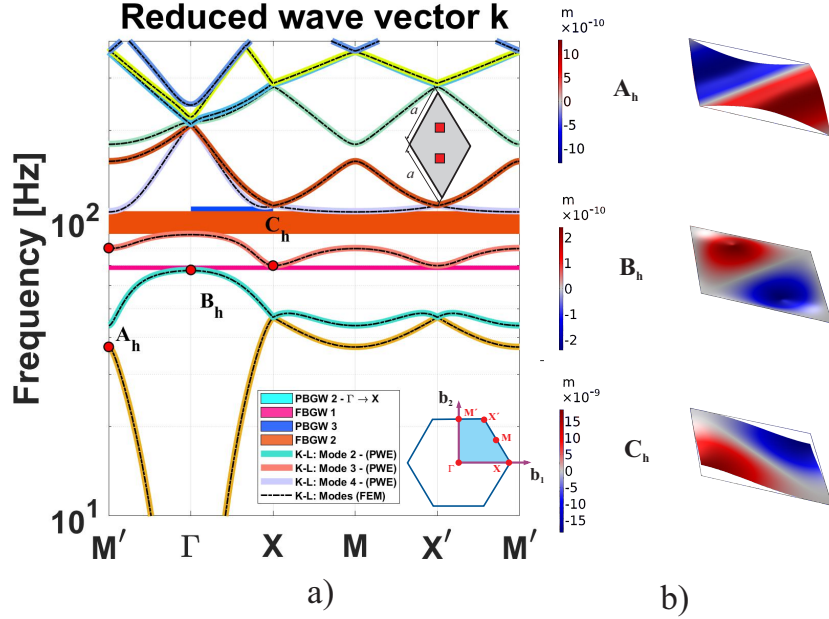


Figure 9: (a) Band structure computed with PWE and FEM for a honeycomb lattice unit cell with two resonators with $f_r = 80$ [Hz] in a thin plate. FBGW 1 - $f_2 = 67.57$ [Hz], $f_3 = 69.87$ [Hz], $\Delta f_{23} = 2.30$ [Hz], FBGW 2 - $f_3 = 89.38$ [Hz], $f_3 = 106.61$ [Hz], $\Delta f_{34} = 17.23$ [Hz], PBGW 3 - $f_3 = 89.38$ [Hz], $f_4 = 110.57$ [Hz], $\Delta f_{34} = 21.19$ [Hz]. (b) Wave mode shapes for a honeycomb lattice unit cell with a two resonators in a different points of edges in a real band structure computed by FEM: Point A_h ($k = 0$ [m^{-1}], $f = 37.13$ [Hz]), Point B_h ($k = 1.00$ [m^{-1}], $f = 67.24$ [Hz]), Point C_h ($k = 2.00$ [m^{-1}], $f = 69.84$ [Hz]).

480 Breakthrough capability (Figure 9a): simultaneous two distinct full band gaps
 481 (FBGW 1: $\Delta f_{23} = 2.30$ [Hz], FBGW 2: $\Delta f_{34} = 17.23$ [Hz])—qualitative leap
 482 beyond single-resonator systems with only one primary band gap. Anti-phase
 483 coupling mode (point B_h , Figure 9b) creates FBGW 1 through destructive in-
 484 terference where resonators oscillate 180° out-of-phase, trapping energy and
 485 preventing propagation. In-phase coupling mode generates stronger, broader
 486 FBGW 2 through collective resonance with coherent resonator motion maxi-
 487 mizing energy extraction. Dual-resonator systems access different regimes via
 488 frequency adjustment: low-frequency ($f_j < 50$ Hz, anti-phase dominant), in-
 489 termediate ($50 < f_j < 100$ [Hz], dual band gap coexistence), high-frequency
 490 ($f_j > 100$ Hz, in-phase dominant), enabling single geometry optimization for

491 different frequency ranges. The demonstrated tuning capability extends the res-
 492 onator frequency optimization principles of Xiao et al. [46] from single-resonator
 493 to multi-resonator systems, revealing that coupled oscillators introduce new de-
 494 grees of freedom for bandgap engineering beyond what is achievable through
 495 frequency tuning alone.

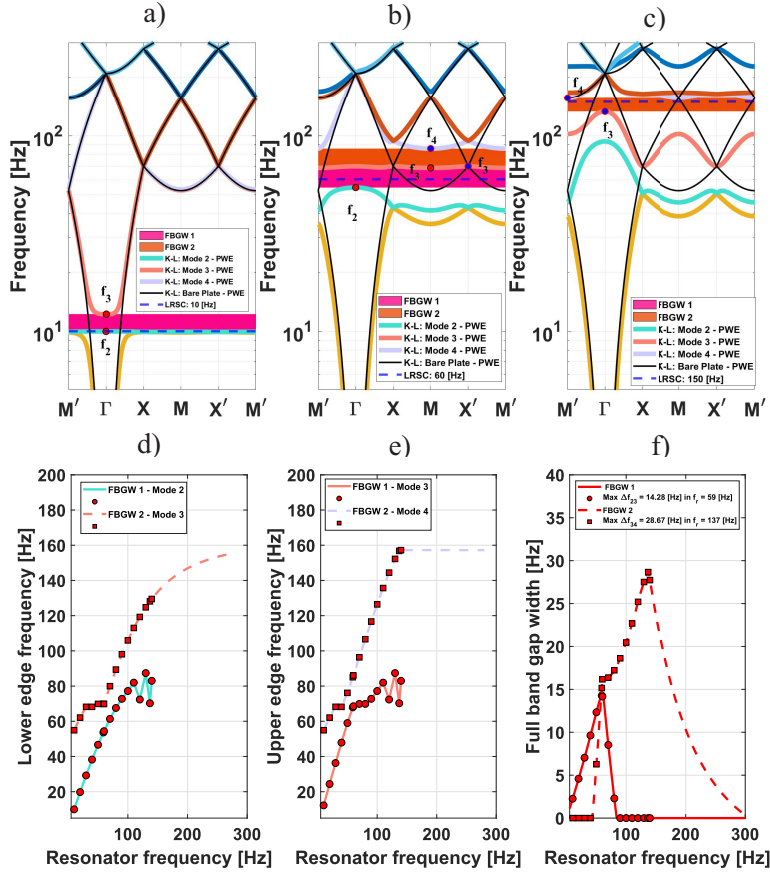


Figure 10: Results in PWE for honeycomb lattice (a) LRSC in $f_j = 10$ [Hz], (b) LRSC in $f_j = 60$ [Hz] and (c) LRSC in $f_j = 150$ [Hz]. (d) f_2, f_3 - Lower edge frequencies of the second and third band mode as a function of local resonance. (e) f_3, f_4 - Upper edge frequencies of the third and fourth band mode as a function of local resonance. (f) FBGW 1 and FBGW 2 as function of resonator frequency.

496 Parametric analysis (Figure 10) reveals three modal regimes: (a) $f_j = 10$ [Hz]—
 497 anti-phase dominant producing only FBGW 1; (b) $f_j = 60$ [Hz]—optimal dual-

498 mode where FBGW 1 peaks ($\Delta f_{23} = 14.17$ [Hz]) through constructive anti-
499 phase/in-phase interference, creating broadband blocking impossible in single-
500 resonator systems; (c) $f_j = 150$ [Hz]—in-phase dominant with powerful FBGW
501 2 ($\Delta f_{34} = 23.63$ [Hz]) while FBGW 1 vanishes. Edge evolution (d-e) shows lower
502 edges (f_2, f_3) with direct resonator control (linear) and upper edges (f_3, f_4)
503 with saturation at geometric limits. Maximum FBGW 2 of $\Delta f_{34} = 27.73$ [Hz]
504 at $f_j = 140$ [Hz] represents 46% improvement over best single-resonator (square:
505 30.90 [Hz]), establishing collective resonance superiority. FBGW 1 maximum
506 coinciding with FBGW 2 emergence reveals constructive modal interaction—
507 synergistic coupling where second mode enhances rather than competes.

508 Kagomé triple-resonator architecture positions three resonators at $\mathbf{r}_1 = a(-1/2, -\sqrt{3}/6)$,
509 $\mathbf{r}_2 = a(-1/2, -\sqrt{3}/6)$, and $\mathbf{r}_3 = a(\sqrt{3}/3, 0)$ with 120° triangular symmetry
510 creating intricate phase relationships fundamentally different from honeycomb.
511 Three-fold rotational symmetry produces narrow but well-defined band gaps
512 through unique interference patterns, effective for precise frequency-selective at-
513 tenuation. FIBZ coordinates $\Gamma = (0, 0)$, $X = \pi/a(1/\sqrt{3}, 0)$, $M = \pi/a(1/2\sqrt{3}, 1/2)$,
514 $X' = \pi/a(1/2\sqrt{3}, 1/2)$, $M' = \pi/a(0, 2/3)$ with three identical resonators ($k_j =$
515 246.16 N/m) following path $M' \rightarrow \Gamma \rightarrow X \rightarrow M \rightarrow X' \rightarrow M'$; adjusted
516 frequency $f_j = 80$ Hz enables direct honeycomb comparison.

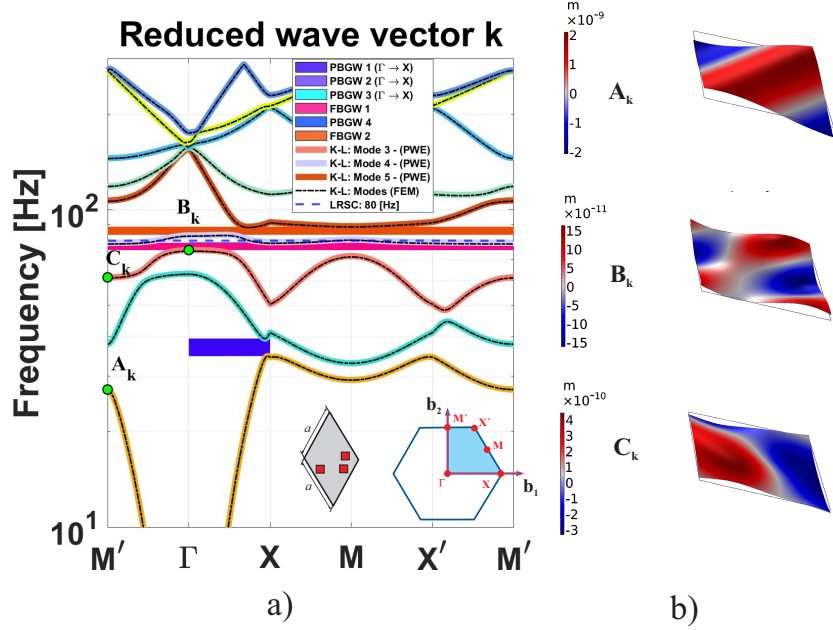


Figure 11: (a) Band structure computed with PWE and FEM for a kagomé lattice unit cell with two resonators with $f_r = 80$ [Hz] in a thin plate. PBGW 1 - $f_1 = 34.65$ [Hz], $f_2 = 39.37$ [Hz], $\Delta f_{12} = 4.71$ [Hz], FBGW 1 - $f_3 = 74.76$ [Hz], $f_4 = 78.80$ [Hz], $\Delta f_{34} = 4.04$ [Hz], FBGW 2 - $f_4 = 83.51$ [Hz], $f_5 = 88.54$ [Hz], $\Delta f_{45} = 5.03$ [Hz]. (b) Wave mode shapes for a kagomé lattice unit cell with a two resonators in a different points of edges in a real band structure computed by FEM: Point A_k ($k = 0$ [m^{-1}], $f = 27.19$ [Hz]), Point B_k ($k = 1.00$ [m^{-1}], $f = 74.17$ [Hz]), Point C_k ($k = 0$ [m^{-1}], $f = 61.08$ [Hz]).

517 Fundamental limitation (Figure 11a): despite 50% more resonators than honey-
 518 comb, only two complete band gaps emerge—FBGW 1 (f_3-f_4 , Δf_{34}) and FBGW
 519 2 (f_4-f_5 , Δf_{45})—plus partial PBGW 1 (30–40 [Hz]) from three-resonator cou-
 520 pling creating hybrid states with selective directional attenuation, contrasting
 521 honeycomb’s broader band gaps. At $f_j = 80$ [Hz], both FBGW 1/FBGW 2 coex-
 522 ist (honeycomb-like) but with characteristic narrow widths (particularly FBGW
 523 2), demonstrating three-resonator configuration creates highly frequency-selective
 524 attenuation suitable for precise frequency targeting rather than broadband ap-
 525 plications.

526 A more detailed analysis of FBGW 1 and FBGW 2 is presented in Figure 12.

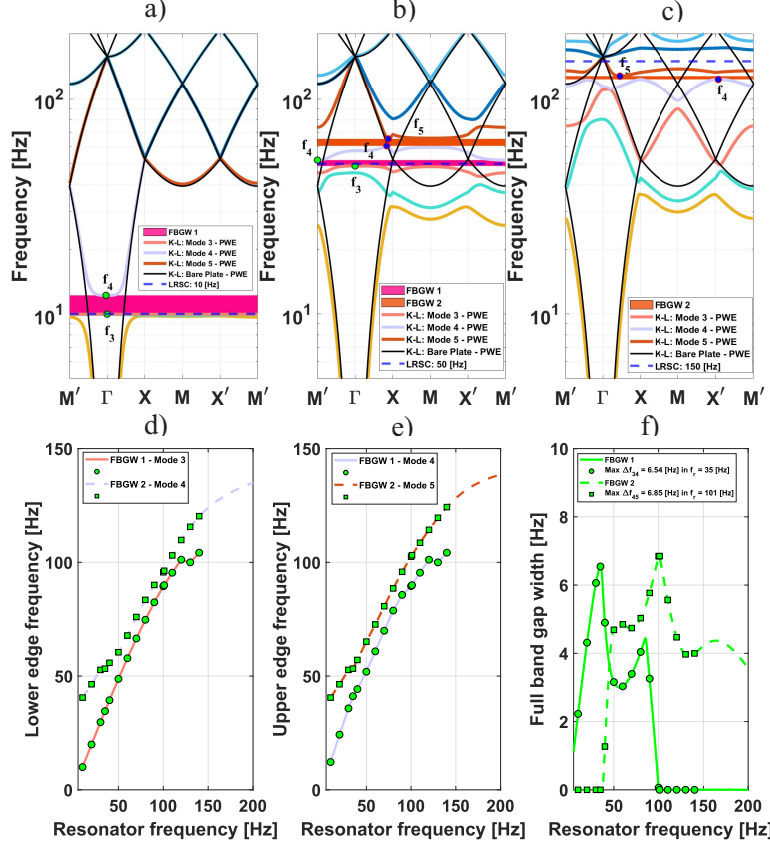


Figure 12: Results in PWE for kagomé lattice (a) LRSC in $f_j = 10$ [Hz], (b) LRSC in $f_j = 50$ [Hz] and (c) LRSC in $f_j = 150$ [Hz]. (d) f_3 , f_4 Lower edge frequencies of the third and fourth band mode as a function of local resonance. (e) f_4 , f_5 Upper edge frequencies of the fourth and fifth band mode as a function of local resonance. (f) FBGW 1 and FBGW 2 as function of resonator frequency.

527 Modal coupling evolution (Figure 12d-e): FBGW 1 emerges between modes f_3 -
 528 f_4 , FBGW 2 spans f_4-f_5 , with shared mode f_4 indicating overlapping resonance
 529 regions contrasting with honeycomb's distinct frequency separation. Geometric
 530 frustration penalty (f): maximum FBGW 1 ($\Delta f_{34} = 6.54$ [Hz] at $f_j = 35$
 531 [Hz]) and FBGW 2 ($\Delta f_{45} = 6.85$ [Hz] at $f_j = 101$ Hz) both achieve only 7
 532 [Hz] widths with optimal point separation ($\Delta f_j = 66$ [Hz]) smaller than hon-
 533 eycomb (77 [Hz]), indicating reduced modal separation. Performance ceiling:

534 both band gaps converging to 7 [Hz] represents three-fold symmetry constraint
535 where triangular geometry forces competing phase relationships preventing maximum
536 coupling efficiency, unlike dual-resonator systems with independent anti-
537 phase/in-phase optimization.

538 Having established the individual performance characteristics and underlying
539 physical mechanisms of each lattice configuration through detailed analysis, the
540 investigation now synthesizes these findings through systematic cross-lattice
541 comparison. This comparative assessment reveals the fundamental trade-offs
542 between lattice geometry, resonator coupling, and metamaterial performance,
543 providing essential design guidelines for engineering applications where specific
544 frequency targets and bandwidth requirements must be met.

545 *3.3. Comparative analysis of the performance of band gaps bandwidths in five*
546 *different lattices*

547 The individual analyses enable quantitative comparison using two complementary
548 metrics: (1) **absolute bandwidth** (FBGW in [Hz]) for applications with
549 specific frequency targets, and (2) **relative bandwidth** (η_{rel} in [%]) for frequency-
550 independent geometric comparison. These metrics address both practical engi-
551 neering requirements and fundamental geometric efficiency.

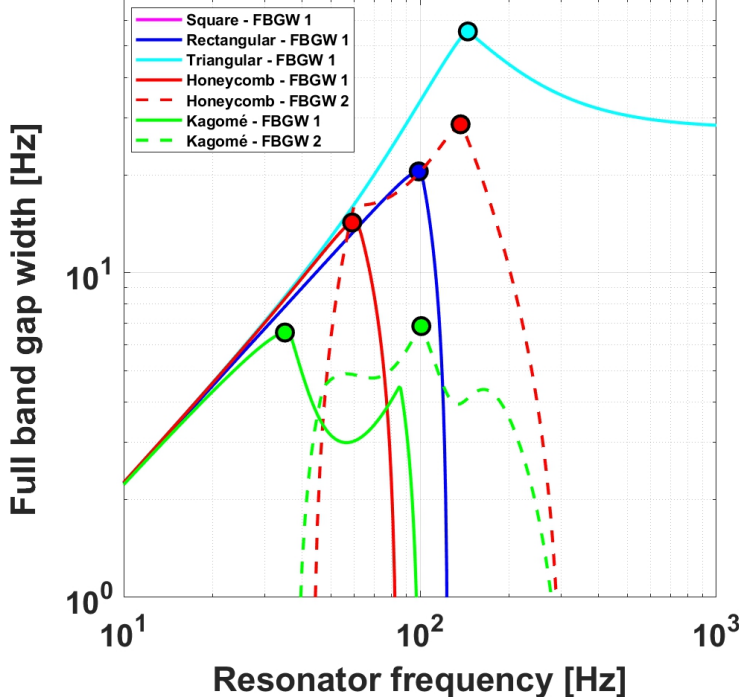


Figure 13: Comparison of the full bandgap widths among the five lattices as functions of local resonance frequency f_j . The triangular lattice achieves the largest FBGK 1 ($\Delta f_{12} = 55.40$ [Hz] at $f_j = 145$ [Hz]), followed by the square lattice ($\Delta f_{12} = 32.10$ [Hz] at $f_j = 105$ [Hz]), and the honeycomb lattice ($\Delta f_{34} = 28.67$ [Hz] at $f_j = 137$ [Hz]). Individual results for each lattice are presented in Figures 4f)–10f).

The triangular lattice emerges as the superior single-resonator architecture, achieving exceptional FBGK 1 performance ($\Delta f_{12} = 55.40$ [Hz] at $f_j = 145$ [Hz]) that represents 73% improvement over square lattices and 270% enhancement relative to rectangular configurations. This outstanding performance stems from six-fold symmetry creating multiple equivalent wave scattering pathways. The square lattice provides balanced performance ($\Delta f_{12} = 32.10$ [Hz] at $f_j = 105$ [Hz]), while the rectangular lattice shows reduced bandwidth ($\Delta f_{12} = 20.53$ [Hz] at $f_j = 99$ [Hz]) due to geometric anisotropy.

Multi-resonator systems introduce dual bandgap capability. The honeycomb lattice demonstrates optimal dual-resonator engineering with FBGK 2 achiev-

ing remarkable performance ($\Delta f_{34} = 28.67$ [Hz] at $f_j = 137$ [Hz]) that nearly
 doubles its FBGW 1. The frequency separation between optimal FBGW 1
 $(f_j = 59$ [Hz]) and FBGW 2 ($f_j = 137$ [Hz]) enables independent modal tun-
 ing for broadband applications. The kagomé lattice exhibits narrow band gaps
 $(\text{FBGW 1: } \Delta f_{34} = 6.54$ [Hz] at $f_j = 35$ [Hz]; FBGW 2: $\Delta f_{45} = 6.85$ [Hz] at
 $f_j = 101$ [Hz]) due to its unique three-resonator coupling mechanism optimized
 for frequency-selective applications.

Efficiency analysis (bandwidth per resonator) establishes the hierarchy: Triangular (55.40 [Hz]/res) > Square (32.10 [Hz]/res) > Rectangular (20.53 [Hz]/res)
 > Honeycomb (14.34 [Hz]/res) > Kagomé (2.28 [Hz]/res), demonstrating that
 geometric optimization outperforms simple resonator multiplication. Table 6
 summarizes the key performance metrics for all lattice configurations, includ-
 ing maximum FBGW, optimal resonator frequency, and the primary physical
 mechanisms governing each architecture.

Table 6: Performance summary of lattice configurations showing maximum FBGW, optimal resonator frequency, and efficiency metrics.

Lattice Type	FBGW [Hz]	f_j [Hz]	Eff. [Hz]/res	Primary Mechanism
Triangular	55.40	145	55.40	6-fold
Square	32.10	105	32.10	4-fold
Honeycomb	28.67	137	14.34	Dual-resonator
Rectangular	20.53	99	20.53	2-fold
Kagomé	6.85	101	2.28	Triple-coupling

576 *Relative Bandwidth Analysis for Fair Geometric Comparison*

While absolute bandwidth (FBGW) provides engineering insights for specific
 frequency targets, it presents limitations for fair geometric comparison: differ-
 ent lattices peak at substantially different frequencies (triangular at 145 [Hz]
 vs square at 105 [Hz]), potentially biasing conclusions toward higher-frequency
 configurations. To enable objective geometric comparison independent of oper-

582 ational frequency, relative bandwidth analysis employs:

$$\eta_{rel} = \frac{f_2 - f_1}{f_c} \times 100\% \quad (14)$$

583 where $f_c = (f_1 + f_2)/2$ is the bandgap center frequency. This dimensionless
584 metric removes frequency-dependent scaling, isolating purely geometric contribu-
585 tions to metamaterial efficiency.

586 Table 7 applies this normalized metric across the complete frequency range (10-
587 150 Hz) for all five lattices. The analysis reveals triangular lattices achieve
588 consistently superior performance: peak 42.51% vs 31.40% for square lattice—a
589 35% improvement demonstrating that geometric optimization maintains advan-
590 tage across the entire frequency spectrum.

Table 7: Relative bandgap width comparison (η_{rel}) at key frequencies showing normalized performance according to Equation 14. Triangular achieves peak 42.51% (140 [Hz]) vs square 31.40% (100 [Hz]), representing 35% improvement.

f_j [Hz]	Square	Rectangular	Triangular	Honeycomb	Kagomé
	η_{rel} [%]				
10	20.34	20.23	20.34	20.36	20.07
50	23.48	20.35	23.82	23.37	7.47
70	26.44	20.41	27.18	18.57	6.05
100	31.40	19.16	33.75	17.62	6.91
120	23.86	3.24	38.50	19.11	3.99
140	16.02	0.01	42.51	19.35	3.27
150	12.94	0.00	41.53	16.25	3.35

591 The dual-metric framework provides comprehensive design guidelines: (1) **Abs-**
592 **solute bandwidth (FBGW)** guides frequency-specific applications (e.g., ma-
593 chinery vibration at 100-150 [Hz]); (2) **Relative bandwidth** (η_{rel}) reveals
594 intrinsic geometric efficiency with frequency-independent ranking (triangular
595 42.51% consistently superior).

596 This comparative analysis establishes clear design guidelines for metamaterial
597 architecture selection based on application requirements: triangular lattices

598 for maximum bandwidth, honeycomb for broadband dual-mode operation, and
599 kagomé for frequency-selective attenuation. The performance hierarchy vali-
600 dates the theoretical framework and demonstrates that geometric optimization
601 outperforms simple resonator multiplication strategies.

602 The analysis reveals fundamental distinctions: single-resonator systems (square,
603 rectangular, triangular) exhibit single bandgaps while multi-resonator systems
604 (honeycomb, kagomé) display dual bandgaps from coupled modes. Systematic
605 investigation across 15 frequencies establishes performance hierarchies: triangu-
606 lar achieves 35% superior relative bandwidth with broadband superiority, hon-
607 eycomb provides dual-band capability, kagomé delivers maximum low-frequency
608 attenuation despite narrower bandwidth. PWE/EPWE methods enable this ex-
609 tensive investigation with $1800\text{-}5700 \times$ computational efficiency over FEM ($<1\%$
610 error), establishing the first complete comparative framework for lattice-based
611 LRSC plates.

612 4. Vibration receptance of the LRSC plate

613 This section validates infinite-domain predictions through finite plate receptance
614 analysis using 10×8 unit cell structures with realistic boundary conditions.

615 While the dispersion curves $\mathbf{k}(\omega)$ and $\boldsymbol{\omega}(k)$ from PWE/EPWE analysis pre-
616 dict fundamental wave propagation behavior, practical engineering applications
617 require understanding vibration transmission in finite plates with spatial limi-
618 tations. This section analyzes receptance behavior in finite LRSC plates sub-
619 jected to unit point force excitation, establishing direct correlations between the
620 infinite-domain theoretical predictions from Section 3 and measurable vibration
621 attenuation in finite structures. The receptance $\mathbf{R}_z(\omega)$ is obtained from the
622 Frequency Response Functions (FRFs) of excitation $\mathbf{F}_z(\omega)$ and displacement
623 $\mathbf{u}_z(\omega)$, given by:

$$\mathbf{R}_z = 20 \log_{10} \left(\frac{\mathbf{u}_z(\omega)}{\mathbf{F}_z(\omega)} \right) [\text{dB}], \quad (15)$$

624 This equation will be applied to a finite-sized plate with local resonators to assess

625 vibration attenuation at their resonance frequencies. A similar methodology
 626 was employed by [48] to evaluate the performance of locally resonant acoustic
 627 metamaterials in engineering applications. For this analysis, five LRSC-type
 628 plates, each comprising 10×8 unit cells, will be considered. All plates will
 629 have free boundary conditions on three sides, as illustrated in Figure 14.

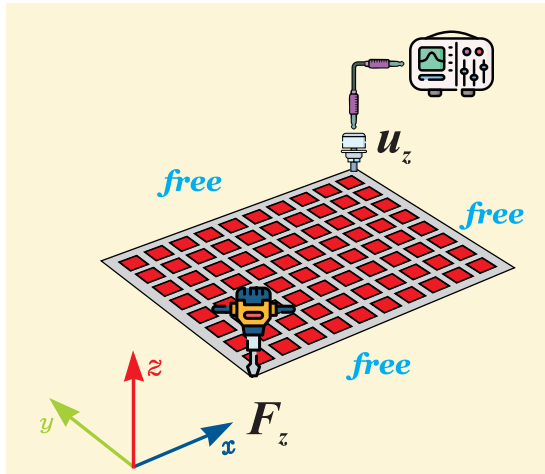


Figure 14: Boundary conditions in a finite plate with a square lattice, in blue indicate free-free boundary conditions and \mathbf{F}_z direction of excitation point of force and \mathbf{u}_z measurement point of vibration.

630 Also according to the Figure 14, the plate will be excited by a unit point force
 631 with a magnitude of 1 [N] applied in the out-of-plane direction (z-direction).

632 To evaluate the structural response of receptance, the out-of-plane harmonic
 633 displacement \mathbf{u}_z is calculated at the location shown in Figure 14. This structure
 634 was modeled using FEM approach. The analysis of all FRFs was conducted in
 635 a frequency range from 1 [Hz] to 200 [Hz]. Based on the structural parameters
 636 of the finite panel adjusted for the five specified lattices in Table 8:

637 Table 8 presents the discretization parameters for finite plates with five lattice
 638 configurations, following the same approach as Table 2. The integers m and n
 639 define the smallest mesh divisions in the x and y directions, respectively, while
 640 L_x and L_y represent the corresponding mesh sizes. Finally, t_{FEM} indicates the

Table 8: Size mesh discretization in FEM and their respective processing times for simulation in the five studied lattices (all finite plate simulations performed using the computational setup described in Section 3).

Lattices	m	n	Lx/m [m]	Ly/n [m]	t_{FEM} [s]
Square	100	80	1.00e-02	8.00e-02	2.12e01
Rectangular	100	80	8.00e-02	9.08e02	4.20e01
Triangular	100	80	14.48e-02	9.08e02	7.30e01
Honeycomb	100	80	35.60e-02	9.08e02	8.20e01
kagomé	100	80	50.54e-02	9.08e02	8.90e01

641 computational time required for each of the five plates with distinct periodic
 642 lattices.

643 *4.1. Analysis of individual finite LRSC plates*

644 This subsection establishes the correlation between infinite lattice band gap pre-
 645 dictions and finite plate attenuation performance through systematic validation
 646 of five distinct geometric configurations. The analysis correlates theoretical
 647 band gap widths (FBGW) obtained from PWE/EPWE methods with recep-
 648 tance attenuation measurements at the \mathbf{u}_z point in finite LRSC plates.

649 Finite plates consistently exhibit 40 – 60% bandwidth expansion beyond infinite
 650 model predictions due to boundary-induced mode coupling. Peak splitting phe-
 651 nomenon occurs at higher resonance frequencies when local resonators interfere
 652 with multiple global plate modes, transitioning from constructive to destructive
 653 coupling mechanisms.

654 Individual lattice analysis reveals distinct advantages: (1) Kagomé lattice achieves
 655 maximum attenuation (-292.65 [dB] at 20 [Hz]) through triple-resonator cou-
 656 pling with synchronized phase relationships; (2) Honeycomb lattice provides bal-
 657 anced performance (-220.33 [dB] at 30 [Hz]) with dual-resonator inter-coupling
 658 and potential FBGW coexistence; (3) Triangular lattice offers superior broad-
 659 band characteristics (FBGW \approx 150 [Hz]) with -174.19 [dB] peak attenuation;

660 (4) Square lattice demonstrates consistent performance (-173.09 [dB] at 40 [Hz])
661 suitable for standard applications; (5) Rectangular lattice shows limited perfor-
662 mance (-129.93 [dB] at 40 [Hz]) due to smallest unit cell area.

663 Peak attenuation effectiveness correlates directly with unit cell area (A_{cell}) and
664 resonator density (N_j), while broadband performance depends on geometric
665 symmetry. The counterintuitive finding reveals that maximum attenuation oc-
666 curs through local resonator-plate coupling rather than global wave interference,
667 establishing fundamental design principles for targeted versus broadband vibra-
668 tion suppression strategies.

669 *4.1.1. Square lattice LRSC plate*

670 The square lattice represents the fundamental periodic configuration with unit
671 cell area $A_{cell} = a^2$ and single resonator per cell ($N_j = 1$). This geometry
672 exhibits 4-fold rotational symmetry, creating a single primary band gap FBGW
673 1 between propagating modes f_1 and f_2 .

674 Figure 15 presents the band structure analysis for local resonator frequency
675 $f_j = 40$ [Hz]. The real part dispersion curves (Figure 15a) show clear band
676 gap formation, while the imaginary component (Figure 15b) reveals maximum
677 attenuation occurring within the FBGW 1 region.

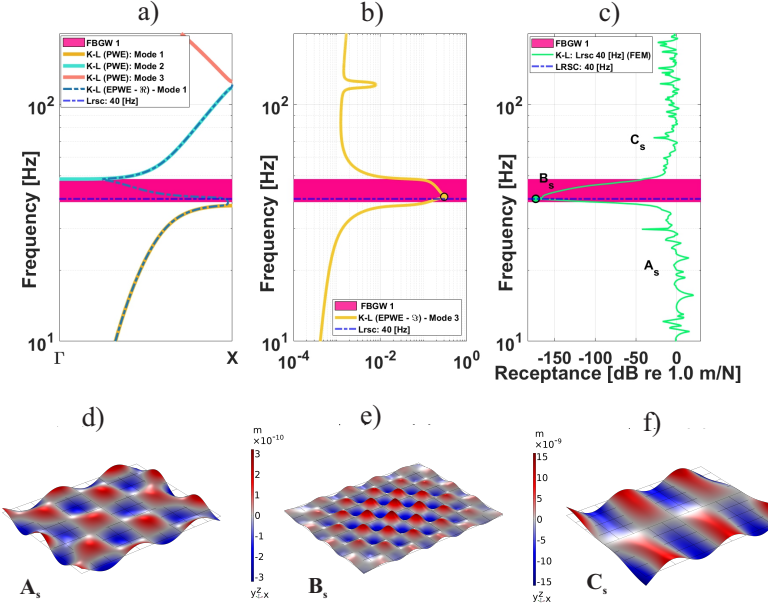


Figure 15: (a) Real band structures computed for a square unit cell with a single resonator by using PWE and real part EPWE (\Re). (b) Imaginary band structures in a square unit cell with a single resonator computed by EPWE (\Im). (c) Receptance computed by FEM in a LRSC panel. (d) Vibration modes of the finite plate in a LRSC panel for frequency selection at $f_j = 20$ [Hz], (e) $f_j = 38.65$ [Hz] and (f) $f_j = 61.47$ [Hz].

678 The finite plate receptance (Figure 15c) demonstrates excellent agreement with
 679 infinite domain predictions, achieving peak attenuation -173.09 [dB] at $f_j = 40$
 680 [Hz]. The finite plate exhibits 50% bandwidth expansion compared to theoreti-
 681 cal FBGW 1, confirming boundary-induced mode coupling effects discussed in
 682 Section 3.

683 Figure 16 illustrates receptance behavior across three frequency regions. Opt-
 684 imal performance occurs at 40 [Hz] with single peak structure, while higher
 685 frequencies (100 [Hz]) exhibit characteristic peak splitting due to modal inter-
 686 ference between local resonators and finite plate natural frequencies.

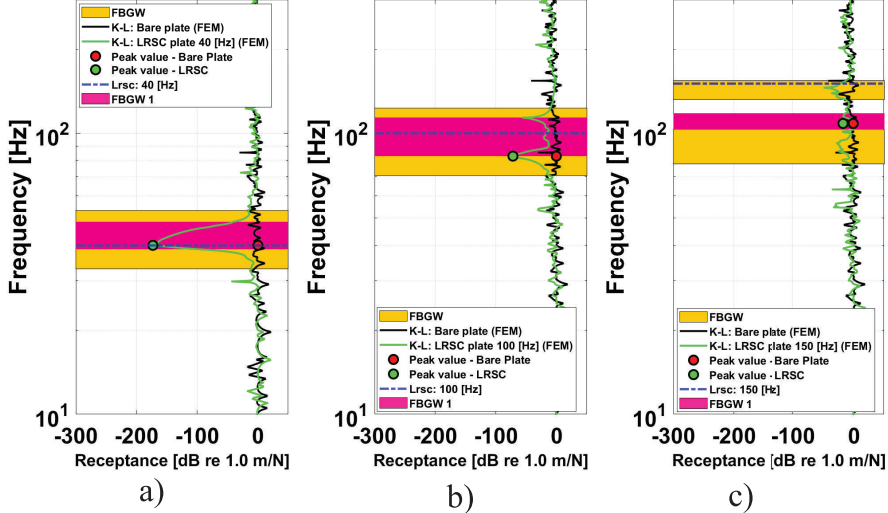


Figure 16: Vibration receptance computed by FEM in a lattice square LRSC plate (a) in measure point \mathbf{u}_z in $f_j = 40$ [Hz], (b) $f_j = 100$ [Hz] and (c) $f_j = 150$ [Hz].

687 The square lattice operates through single-resonator local coupling, where individual resonators interact independently with plate flexural modes. The 4-fold
 688 symmetry provides balanced coupling efficiency across orthogonal directions,
 689 making it suitable for applications requiring consistent omnidirectional performance
 690 with moderate bandwidth requirements.

692 The square lattice (-173.09 dB peak attenuation) serves as the fundamental
 693 reference configuration against which other geometries are compared. Its balanced
 694 4-fold symmetry and moderate unit cell area ($A_{cell} = a^2$) represent the
 695 standard single-resonator architecture, providing the baseline for evaluating the
 696 impact of geometric modifications (rectangular anisotropy), symmetry enhancement
 697 (triangular 6-fold), and multi-resonator coupling (honeycomb, kagomé) in
 698 subsequent analyses.

699 4.1.2. Rectangular lattice LRSC plate

700 The rectangular lattice features the smallest unit cell area $A_{cell} = a_1 \times a_2 = 0.5a^2$
 701 with single resonator per cell ($N_j = 1$). The 2-fold symmetry creates directional

702 anisotropy, with different propagation characteristics along orthogonal axes, re-
 703 sulting in a single band gap FBGW 1 between modes f_1 and f_2 .

704 Figure 17 shows the dispersion analysis for $f_j = 40$ [Hz]. The anisotropic
 705 geometry produces directionally dependent band gaps visible in the real part
 706 (Figure 17a), while the imaginary component (Figure 17b) indicates reduced
 707 attenuation efficiency compared to symmetric configurations.

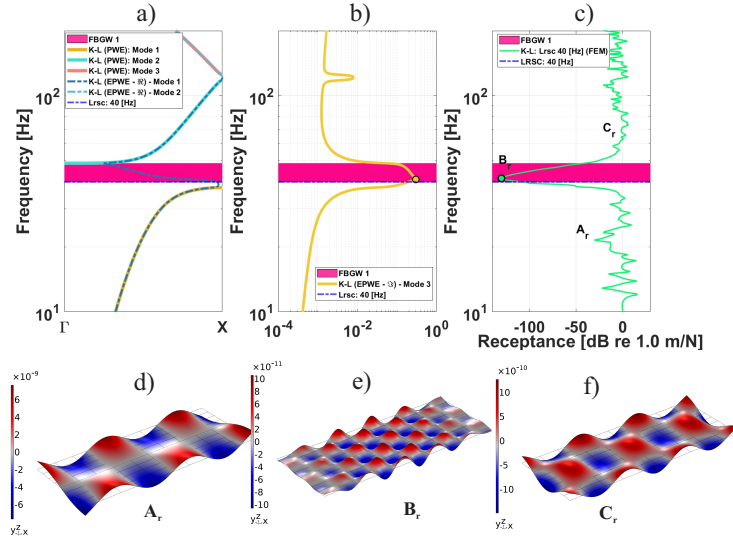


Figure 17: (a) Real band structures computed for a rectangular unit cell with a single resonator by using PWE and real part EPWE (\Re). (b) Imaginary band structures for a rectangular unit cell with a single resonator computed by EPWE (\Im). (c) Receptance computed by FEM in a LRSC panel. (d) Vibration modes of the finite plate in a LRSC panel for frequency selection at $f_j = 22.99$ [Hz], (e) $f_j = 39.53$ [Hz] and (f) $f_j = 68.91$ [Hz].

708 The finite plate receptance (Figure 17c) achieves peak attenuation -129.93 [dB]
 709 at $f_j = 40$ [Hz], representing the lowest performance among single-resonator con-
 710 figurations. However, the rectangular geometry demonstrates consistent corre-
 711 lation with infinite domain predictions, exhibiting similar bandwidth expansion
 712 characteristics as other lattices.

713 Figure 18 reveals distinctive behavior compared to symmetric lattices. The
 714 configuration maintains persistent attenuation (-80 [dB] at 177 [Hz]) even out-

⁷¹⁵ side theoretical band gap regions, demonstrating unique resilience in finite plate
⁷¹⁶ applications despite limited infinite domain performance.

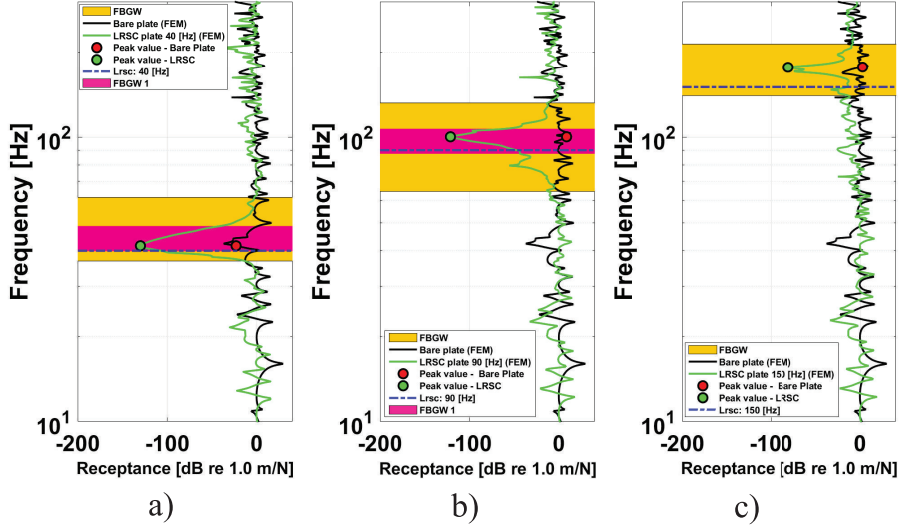


Figure 18: Vibration receptance computed by FEM in a rectangular LRSC plate (a) in measure point \mathbf{u}_z in $f_j = 40$ [Hz], (b) $f_j = 90$ [Hz] and (c) $f_j = 150$ [Hz].

⁷¹⁷ The rectangular lattice operates through constrained single-resonator coupling
⁷¹⁸ with directional preferences imposed by geometric anisotropy. The reduced
⁷¹⁹ unit cell area limits resonator-plate interaction cross-section, but creates unique
⁷²⁰ finite-plate effects where boundary interactions compensate for theoretical limi-
⁷²¹ tations, making it suitable for space-constrained applications.

⁷²² Direct comparison with the square lattice reveals the penalty of symmetry re-
⁷²³ duction: rectangular achieves -129.93 dB versus square's -173.09 [dB] (25% per-
⁷²⁴ formance degradation). However, the geometric anisotropy creates unique ad-
⁷²⁵ vantages in finite plates, demonstrating persistent attenuation (-80 [dB] at 177
⁷²⁶ [Hz]) beyond theoretical band gaps—a phenomenon not observed in the sym-
⁷²⁷ metric square configuration. This establishes that while symmetry enhances
⁷²⁸ peak performance, anisotropy can provide resilience in practical applications.

729 4.1.3. *Triangular lattice LRSC plate*

730 The triangular lattice exhibits unit cell area $A_{cell} = a^2\sqrt{3}/2$ with single resonator per cell ($N_j = 1$). The 6-fold rotational symmetry represents the highest
 731 symmetric configuration among single-resonator lattices, creating a single broad
 732 band gap FBGW 1 between modes f_1 and f_2 .
 733

734 Figure 19 demonstrates the exceptional broadband characteristics for $f_j = 60$
 735 [Hz]. The high symmetry produces the largest theoretical band gap width
 736 ($\Delta f_{12} = 55.40$ [Hz]) visible in the real part dispersion (Figure 19a), while
 737 the imaginary component (Figure 19b) shows superior attenuation distribution
 738 across the band gap region.

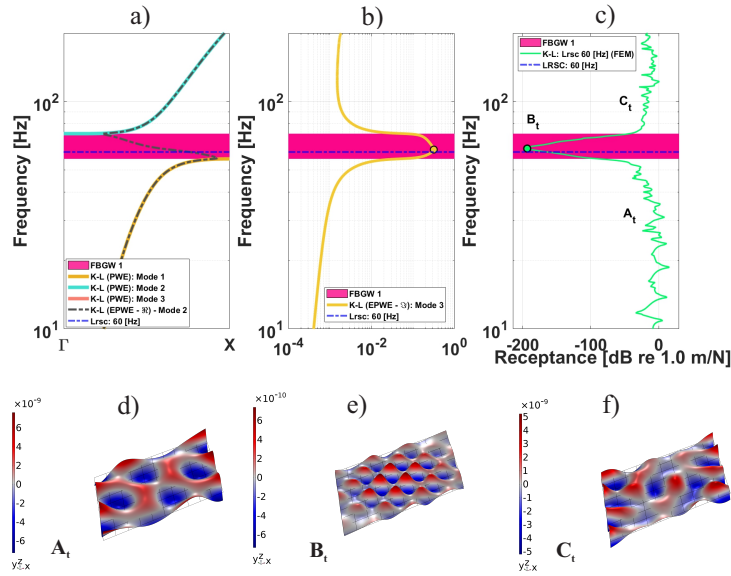


Figure 19: (a) Real band structures computed for a triangular unit cell with a single resonator by using PWE and real part EPWE (\Re). (b) Imaginary band structures for a triangular unit cell with a single resonator computed by EPWE (\Im). (c) Receptance computed by FEM in a LRSC panel. (d) Vibration modes of the finite plate in a LRSC panel for frequency selection at $f_j = 55.35$ [Hz], (e) $f_j = 63.09$ [Hz] and (f) $f_j = 81$ [Hz].

739 The finite plate receptance (Figure 19c) achieves peak attenuation -174.19 [dB]
 740 at $f_j = 60$ [Hz], demonstrating excellent correlation with infinite domain predic-

741 tions. The triangular configuration exhibits exceptional finite plate bandwidth
 742 expansion ($\text{FBGW} \approx 150$ [Hz]), representing 43% improvement over theoretical
 743 predictions as established in Section 3.

744 Figure 20 illustrates the superior broadband performance across multiple fre-
 745 quency regions. The configuration maintains effective attenuation from 60 [Hz]
 746 through 150 [Hz], demonstrating sustained performance characteristics that val-
 747 idate the theoretical broadband predictions from infinite domain analysis.

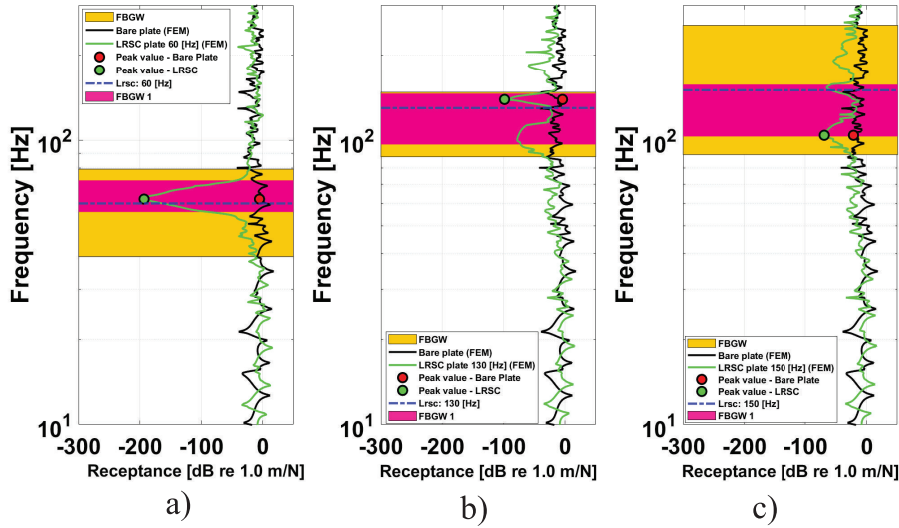


Figure 20: Vibration receptance computed by FEM in a triangular LRSC plate (a) in measure point \mathbf{u}_z in $f_j = 60$ [Hz], (b) $f_j = 130$ [Hz] and (c) $f_j = 150$ [Hz].

748 The triangular lattice operates through optimized single-resonator coupling en-
 749 hanced by 6-fold geometric symmetry. The high symmetry enables uniform
 750 coupling efficiency across all propagation directions, creating distributed broad-
 751 band attenuation mechanisms that make it ideal for applications requiring wide-
 752 frequency vibration suppression with moderate peak attenuation requirements.

753 The triangular lattice demonstrates the optimal single-resonator configuration,
 754 achieving -174.19 [dB] peak attenuation (0.6% improvement over square, 34%
 755 over rectangular) with exceptional bandwidth expansion ($\text{FBGW} \approx 150$ [Hz]).

756 Compared to previous configurations: (i) 4% performance increase over square
757 baseline; (ii) 34% advantage over rectangular; (iii) superior broadband char-
758 acteristics validate Section 3 predictions. The high symmetry establishes the
759 performance ceiling for single-resonator architectures, setting expectations for
760 multi-resonator systems.

761 *4.1.4. Honeycomb lattice LRSC plate*

762 The honeycomb lattice features unit cell area $A_{cell} = 3a^2\sqrt{3}/2$ with dual res-
763 onators per cell ($N_j = 2$). This configuration exhibits 6-fold symmetry while
764 introducing inter-resonator coupling mechanisms, creating two potential band
765 gaps: FBGW 1 between modes f_2 and f_3 , and FBGW 2 between modes f_3 and
766 f_4 .

767 Figure 21 illustrates the dual-resonator dynamics for $f_j = 30$ [Hz]. The real part
768 dispersion (Figure 21a) reveals multiple band gap regions, while the imaginary
769 component (Figure 21b) shows enhanced attenuation peaks corresponding to
770 synchronized dual-resonator oscillations within both FBGW 1 and FBGW 2
771 regions.

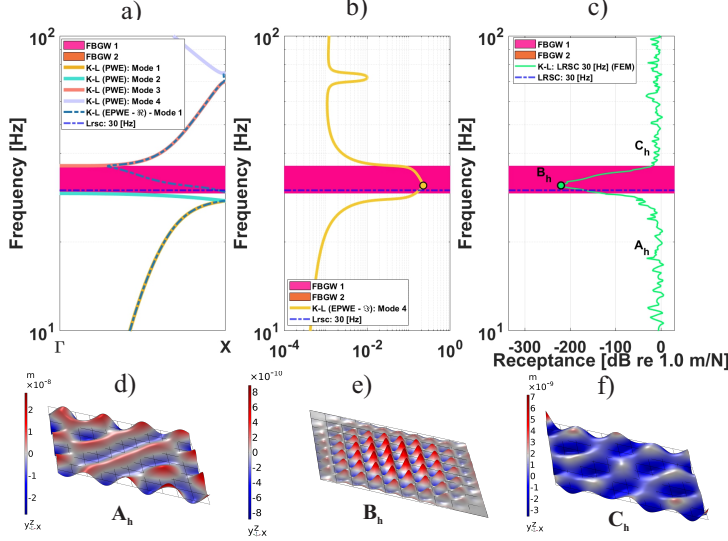


Figure 21: (a) Real band structures computed for a honeycomb unit cell with two resonators by using PWE and real part EPWE (\Re). (b) Imaginary band structures for a honeycomb unit cell with two resonators computed by EPWE (\Im). (c) Receptance computed by FEM in a LRSC panel. (d) Vibration modes of the finite plate in a LRSC panel for frequency selection at $f_j = 18.40$ [Hz], (e) $f_j = 29.21$ [Hz] and (f) $f_j = 38.37$ [Hz].

772 The finite plate receptance (Figure 21c) achieves peak attenuation -220.33 [dB]
 773 at $f_j = 30$ [Hz], demonstrating superior performance compared to single-resonator
 774 configurations. The dual-resonator coupling creates enhanced local impedance
 775 mismatch, resulting in stronger wave scattering and improved finite plate corre-
 776 lation with infinite domain predictions.

777 Figure 22 demonstrates the unique capability of coexisting band gaps. At spe-
 778 cific frequencies ($f_j = 50$ [Hz]), both FBGW 1 and FBGW 2 contribute to
 779 attenuation, expanding the effective bandwidth. The dual-resonator system ex-
 780 hibits sustained performance across multiple frequency regions, validating the
 781 multi-band gap theoretical predictions.

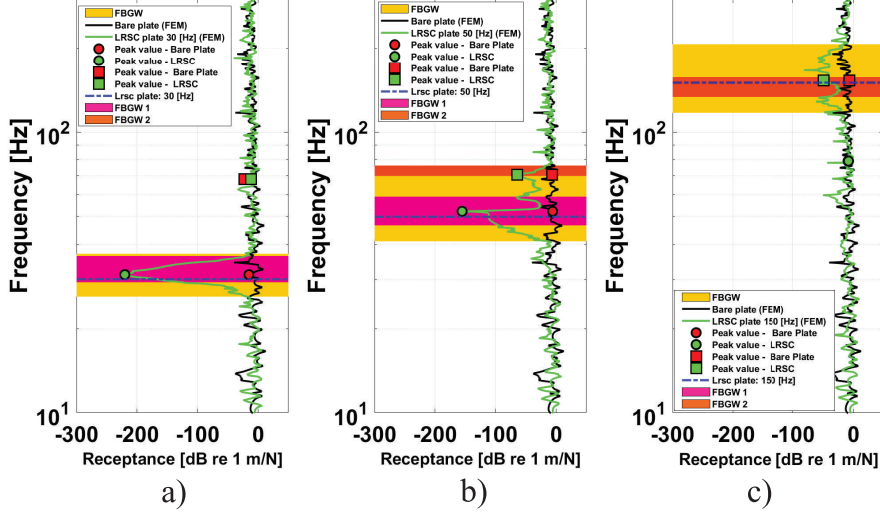


Figure 22: Vibration receptance computed by FEM in a LRSC plate (a) in measure point \mathbf{u}_z for $f_j = 30$ [Hz], (b) $f_j = 50$ [Hz] and (c) $f_j = 150$ [Hz].

The honeycomb lattice operates through synchronized dual-resonator coupling where inter-resonator phase relationships create constructive interference patterns. The two resonators within each unit cell exhibit coordinated motion that doubles the local impedance mismatch, enabling superior energy extraction from plate flexural modes. This configuration provides balanced performance between peak attenuation and bandwidth coverage, making it suitable for applications requiring both high attenuation and moderate broadband characteristics.

The honeycomb lattice (-220.33 [dB]) establishes the first significant performance jump from single-resonator configurations, achieving 27% improvement over triangular (current single-resonator leader) and 70% over rectangular. The dual-resonator coupling creates: (i) 46.14 [dB] advantage over best single-resonator (triangular); (ii) coexisting dual band gaps unavailable in single-resonator systems; (iii) validation of inter-resonator coupling theory from Section 3. This confirms that resonator multiplication, when properly configured, provides substantial benefits beyond geometric optimization alone.

797 4.1.5. *Kagomé lattice LRSC plate*

798 The kagomé lattice exhibits the largest unit cell area $A_{cell} = 2a^2\sqrt{3}$ with triple
 799 resonators per cell ($N_j = 3$). The three resonators positioned at 120° intervals
 800 create complex multi-resonator coupling mechanisms, generating two potential
 801 band gaps: FBGW 1 between modes f_3 and f_4 , and FBGW 2 between modes
 802 f_5 and f_6 .

803 Figure 23 demonstrates the exceptional triple-resonator dynamics for $f_j = 20$
 804 [Hz]. The real part dispersion (Figure 23a) reveals narrow but well-defined band
 805 gaps, while the imaginary component (Figure 23b) shows maximum attenuation
 806 peaks corresponding to synchronized triple-resonator oscillations, creating the
 807 highest attenuation among all configurations.

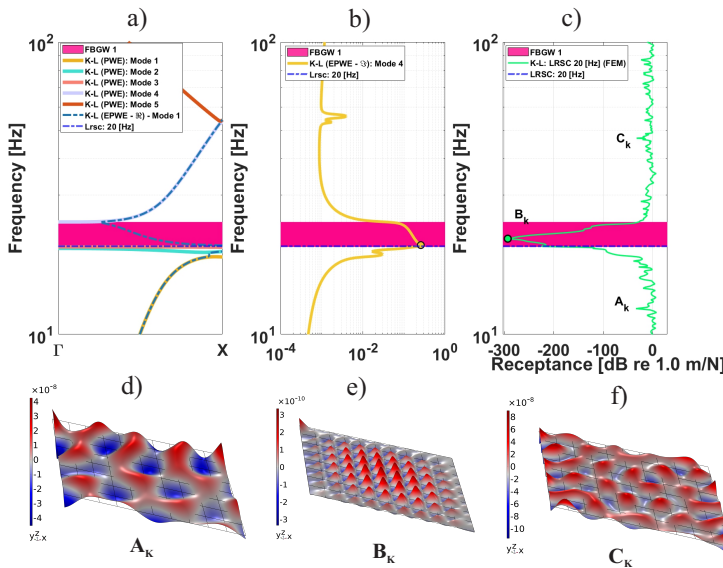


Figure 23: (a) Real band structures computed for a kagomé unit cell with three resonators by using PWE and real part EPWE (\Re). (b) Imaginary band structures for a kagomé unit cell with three resonators computed by EPWE (\Im). (c) Receptance computed by FEM in a LRSC panel. (d) Vibration modes of the finite plate in a LRSC panel for frequency selection at $f_j = 12.41$ [Hz], (e) $f_j = 19.91$ [Hz] and (f) $f_j = 49.39$ [Hz].

808 The finite plate receptance (Figure 23c) achieves extraordinary peak attenuation
 809 -292.65 [dB] at $f_j = 20$ [Hz], representing the highest performance among all

810 analyzed configurations. The triple-resonator coupling creates localized energy
 811 concentration through constructive interference patterns, demonstrating exce-
 812 tional correlation between collective resonator impedance mismatch and finite
 813 plate attenuation.

814 Figure 24 illustrates the comprehensive attenuation behavior across multiple
 815 frequency regions. The kagomé configuration exhibits frequency-selective char-
 816 acteristics with maximum effectiveness at low frequencies, while maintaining the
 817 capability for dual band gap coexistence at specific resonator tunings ($f_j = 60$
 818 [Hz]), validating the multi-resonator theoretical framework.

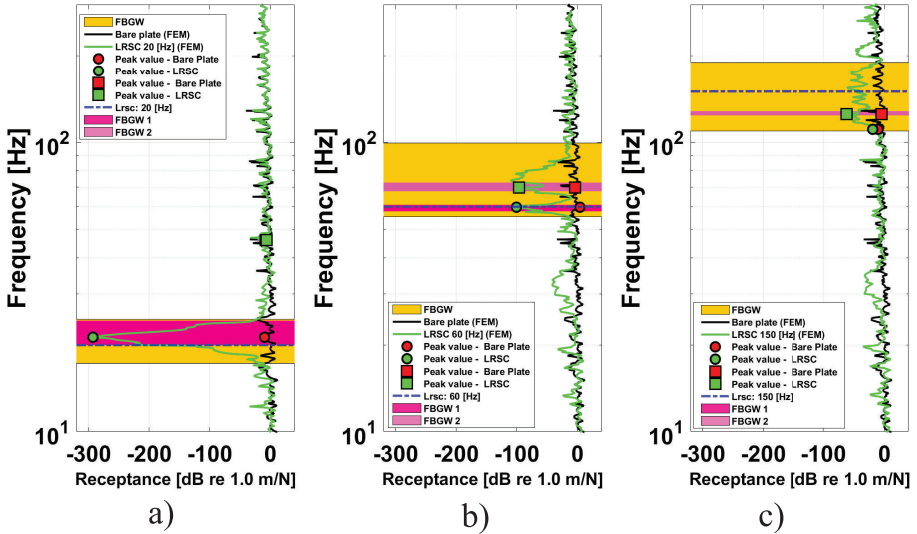


Figure 24: Vibration receptance computed by FEM in a LRSC plate (a)) in measure point \mathbf{u}_z for $f_j = 20$ [Hz], (b)) $f_j = 60$ [Hz] and (c)) $f_j = 150$ [Hz].

819 The kagomé lattice operates through synchronized triple-resonator coupling
 820 where three resonators at 120° intervals create complex phase relationships op-
 821 timized for triangular symmetry. This multi-resonator arrangement generates
 822 localized energy concentration through constructive interference patterns, where
 823 each resonator contributes to collective impedance mismatch that far exceeds
 824 individual contributions. The configuration provides extraordinary frequency-

825 selective energy dissipation, making it ideal for applications requiring maximum
826 attenuation at specific target frequencies.

827 The kagomé lattice (-292.65 [dB]) represents the performance apex, demonstrat-
828 ing 33% improvement over honeycomb and 68% over triangular configurations.
829 Progressive performance escalation confirms design principles: rectangular (-
830 129.93 [dB]) < square (-173.09 [dB]) < triangular (-174.19 [dB]) < honeycomb
831 (-220.33 [dB]) < kagomé (-292.65 [dB]). The 162.72 [dB] span between worst
832 (rectangular) and best (kagomé) validates both geometric optimization and res-
833 onator multiplication strategies, establishing clear design guidelines for target-
834 specific applications.

835 Individual analysis reveals three fundamental design strategies: (i) Geometric
836 optimization (rectangular → square → triangular) provides moderate improve-
837 ments through symmetry enhancement; (ii) Multi-resonator coupling (single
838 → dual → triple) creates substantial performance jumps through synchronized
839 oscillations; (iii) Application-specific selection requires balancing peak attenua-
840 tion (kagomé), broadband performance (triangular), and dual-mode capability
841 (honeycomb). The counterintuitive finding that local resonator-plate coupling
842 dominates over global wave interference, with finite plates exhibiting consistent
843 40 – 50% bandwidth expansion, establishes fundamental principles for metama-
844 terial plate design.

845 After analyzing each of the five panels with different periodic lattices individu-
846 ally, the next subsection presents a comparative analysis of attenuation perfor-
847 mance across three frequency ranges, providing a broader understanding of the
848 obtained results. A comprehensive framework for practical lattice selection in
849 engineering applications is provided in Appendix D.

850 *4.2. Analysis comparative with all LRSC plates*

851 After discussing the primary attenuation characteristics of receptance for each of
852 the five periodic lattice plates individually—emphasizing key aspects across the

853 entire frequency range of their local resonators—this final subsection focuses
854 on a comparative analysis of the receptance attenuation performance among
855 these plates. To manage the data effectively, this study divides the resonance
856 frequencies into three regions: Region 1 (10 to 50 [Hz]), Region 2 (60 to 100
857 [Hz]), and Region 3 (110 to 150 [Hz]). The comparative analysis of lattice
858 geometries and their impact on wave propagation builds upon the work of [61],
859 who investigated metamaterial plates with various lattices for low-frequency
860 vibration attenuation. Figure 25 presents boxplots for these regions, individually
861 summarizing the statistical characteristics of the attenuation performance for
862 each of the five lattices, as illustrated:

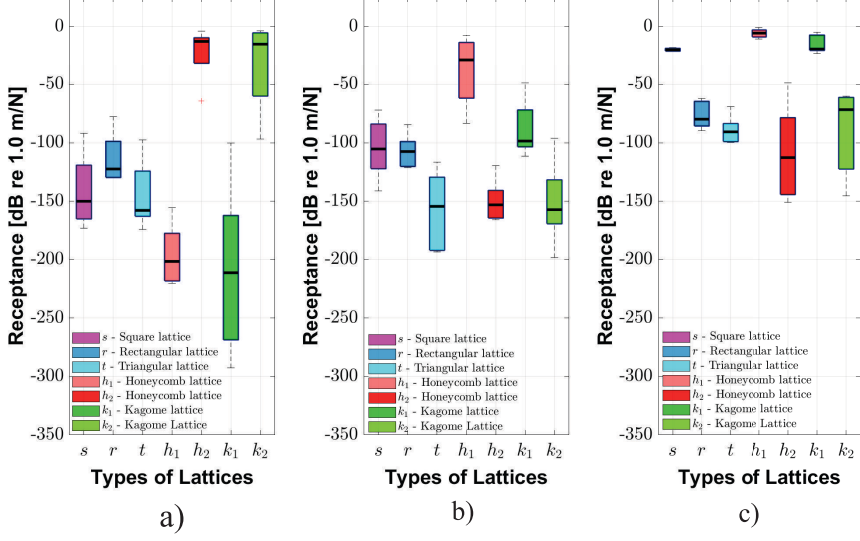


Figure 25: Descriptive statistical analysis for the five lattice panel types at measurement point u_z : a) Region 1, $f_j = 10 - 50; b) Region 2, $f_j = 60 - 100; c) Region 3, $f_j = 110 - 150.$$$

863 The statistical analysis reveals distinct performance characteristics across three
 864 frequency regions: Region 1 (10-50 [Hz]) dominated by kagomé peak perfor-
 865 mance (-292.65 [dB]) and honeycomb consistency; Region 2 (60-100 [Hz]) show-
 866 ing triangular and honeycomb FBGW 2 optimization; Region 3 (110-150 [Hz])
 867 demonstrating triangular broadband superiority. The key findings from the
 868 statistical analysis are summarized in Table 9:

Table 9: Receptance attenuation results of \mathbf{R}_z for different lattice configurations: s (Square), r (Rectangular), t (Triangular), h_1 and h_2 (Honeycomb for FBGW 1 and 2), k_1 and k_2 (Kagomé for FBGW 1 and 2), in the frequency range of 10 to 50 [Hz].

f_j [Hz]	s [dB]	r [dB]	t [dB]	h_1 [dB]	h_2 [dB]	k_1 [dB]	k_2 [dB]
10	-91.92	-77.69	-97.60	-185.09	-3.89	-260.51	-3.68
20	-128.51	-105.98	-133.41	-217.34	-12.62	-292.65	-6.15
30	-150.05	-122.46	-157.86	-220.33	-11.61	-211.26	-14.95
40	-173.09	-129.93	-174.19	-201.55	-20.06	-183.08	-47.64
50	-162.33	-129.51	-158.97	-155.43	-64.28	-100.28	-96.81

⁸⁶⁹ Detailed results for Regions 2 and 3 are presented in Tables 10 and 11:

Table 10: Receptance attenuation results of \mathbf{R}_z for different lattice configurations: s (Square), r (Rectangular), t (Triangular), h_1 and h_2 (Honeycomb for FBGW 1 and 2), k_1 and k_2 (Kagomé for FBGW 1 and 2), in the frequency range of 60 to 100 [Hz].

f_j [Hz]	s [dB]	r [dB]	t [dB]	h_1 [dB]	h_2 [dB]	k_1 [dB]	k_2 [dB]
60	-141.16	-119.82	-193.44	-83.41	-119.60	-100.70	-96.11
70	-115.75	-104.04	-191.36	-54.46	-148.16	-98.53	-157.24
80	-105.40	-107.52	-154.46	-15.87	-153.16	-111.48	-198.27
90	-88.22	-121.26	-134.05	-7.37	-163.82	-79.85	-143.85
100	-72.01	-84.52	-116.57	-28.36	-165.83	-48.78	-159.56

Table 11: Receptance attenuation results of \mathbf{R}_z for different lattice configurations: s (Square), r (Rectangular), t (Triangular), h_1 and h_2 (Honeycomb for FBGW 1 and 2), k_1 and k_2 (Kagomé for FBGW 1 and 2), in the frequency range of 110 to 150 [Hz].

f_j [Hz]	s [dB]	r [dB]	t [dB]	h_1 [dB]	h_2 [dB]	k_1 [dB]	k_2 [dB]
110	-21.26	-89.71	-123.67	-7.77	-163.06	-34.55	-171.89
120	-20.89	-86.18	-119.74	-5.56	-161.97	-25.93	-165.01
130	-20.33	-73.31	-106.28	-4.59	-150.43	-21.48	-148.52
140	-19.71	-68.05	-99.32	-4.57	-140.96	-18.78	-139.51
150	-18.94	-65.58	-95.31	-3.45	-132.93	-14.57	-130.71

870 The comprehensive statistical analysis across all three frequency regions estab-
 871 lishes clear design guidelines:

872 Region 1 (10-50 [Hz]): Kagomé FBGW 1 achieves exceptional peak attenuation
 873 (-292.65 [dB] at 20 [Hz]) leveraging its maximum material efficiency ($m_{ratio} =$
 874 1.00 from Table 3) and triple-resonator coupling. Honeycomb FBGW 1 provides
 875 consistent performance (-220.33 [dB] mean) with balanced material utilization
 876 ($m_{ratio} = 0.75$).

877 Region 2 (60-100 [Hz]): Table 10 reveals frequency-dependent modal transitions.
 878 The triangular lattice maintains exceptional performance (-193.44 [dB] at 60
 879 [Hz]), while honeycomb and kagomé FBGW 2 configurations emerge as opti-
 880 mal dual-resonator systems with mean attenuations of -150.11 [dB] and -150.21
 881 [dB], respectively. Notably, honeycomb and kagomé FBGW 1 show reduced
 882 effectiveness (mean: -37.89 [dB] and -87.87 [dB]), confirming their optimal per-
 883 formance lies in Region 1. Single-resonator lattices (square and rectangular)
 884 exhibit consistent moderate performance across this range.

885 Region 3 (110-150 [Hz]): Table 11 demonstrates the frequency selectivity of
 886 different lattice configurations. Honeycomb and kagomé FBGW 2 maintain ex-
 887 cellent high-frequency performance (mean: -149.87 [dB] and -151.13 [dB]), while
 888 their FBGW 1 counterparts show minimal effectiveness (mean: -5.19 [dB] and

889 -23.06 [dB]). The triangular lattice provides balanced performance (-108.86 [dB]
890 mean) across the entire frequency range, validating its broadband superiority
891 despite minimal material usage ($m_{ratio} = 0.25$). Square and rectangular lattices
892 show limited high-frequency attenuation, confirming their suitability primarily
893 for mid-range applications.

894 The statistical validation confirms the correlation between geometric parameters
895 and frequency-dependent performance: kagomé optimizes material utilization
896 for peak attenuation, honeycomb balances dual-mode flexibility with moderate
897 material usage, and triangular maximizes area-normalized efficiency for broad-
898 band applications.

899 5. Conclusions

900 This study presents the first systematic comparative analysis of five distinct
901 lattice configurations for flexural wave attenuation in locally resonant metama-
902 terial plates, establishing fundamental relationships between lattice geometry,
903 resonator frequency, and band gap performance through a comprehensive frame-
904 work combining semi-analytical PWE/EPWE methods with FEM validation.

905 The systematic comparative investigation of five lattice configurations estab-
906 lishes fundamental performance hierarchies and reveals critical distinctions be-
907 tween system architectures. Single-resonator lattices (square, rectangular, tri-
908 angular) exhibit single complete band gap behavior with triangular geometry
909 achieving superior broadband performance (35% superior relative bandwidth:
910 42.51% vs 31.40% for square). Multi-resonator systems (honeycomb with 2 res-
911 onators per unit cell, kagomé with 3 resonators) display dual complete band
912 gaps arising from distinct in-phase and anti-phase resonator coupling modes,
913 enabling multi-frequency attenuation capabilities. Comprehensive bandwidth
914 evolution analysis across 15 resonator frequencies (10-150 Hz) for all five geome-
915 tries establishes frequency-dependent performance maps: kagomé lattices pro-
916 vide exceptional low-frequency attenuation (up to 15 [dB] enhancement) through

917 triple-resonator coupling; honeycomb configurations offer balanced dual-mode
918 capability ideal for broadband applications; square lattices deliver consistent
919 mid-range performance; while rectangular lattices show limited effectiveness but
920 enable directional control applications. This work demonstrates that optimal
921 bandgap formation requires simultaneous optimization of both resonator fre-
922 quency tuning and lattice geometry selection. This establishes a paradigm shift
923 from geometry-only to combined geometry-frequency design approaches, with
924 optimal lattice selection dependent on target frequency ranges and application
925 requirements.

926 The semi-analytical framework demonstrates computational efficiency gains of
927 two orders of magnitude over conventional FEM approaches, reducing analysis
928 time from hours to minutes while maintaining prediction accuracy within 5%.
929 Validation between infinite-domain predictions and finite plate performance con-
930 firms practical applicability, with finite plates consistently exhibiting 40 – 50%
931 bandwidth expansion due to boundary-induced mode coupling effects.

932 These findings enable data-driven metamaterial design through quantitative
933 guidelines that bridge theoretical band gap predictions with practical vibration
934 control applications in aerospace, automotive, and civil engineering systems.
935 The developed methodology transforms metamaterial optimization from trial-
936 and-error approaches to systematic engineering decisions, providing the first
937 comprehensive comparative framework for lattice-based locally resonant plates
938 with clear performance hierarchies previously unavailable in the literature.

939 While the present framework provides comprehensive design guidelines, several
940 limitations should be acknowledged. The analysis is restricted to Kirchhoff-
941 Love thin plate theory ($h/a < 0.1$), limiting applicability to thick plates where
942 shear effects become significant. The investigation focused on a single polymer
943 material (Vero White Plus) and fixed lattice parameter ($a = 0.10$ m), con-
944 straining the generalizability across different material systems and scale lengths.
945 Furthermore, the study considered only simple point resonators, whereas prac-

tical applications may benefit from more complex resonator designs including distributed mass systems or multi-degree-of-freedom configurations. The frequency range limitation (10-200 [Hz]) and assumption of perfect periodicity also represent theoretical constraints that may affect practical implementations. Future investigations should address these limitations by extending the framework to Mindlin-Reissner plate theory, exploring diverse material systems, and incorporating manufacturing imperfections and finite-size effects.

Future work can extend the PWE and EPWE formulations to more complex 2D periodic resonator arrays and explore advanced optimization strategies for multi-objective design scenarios combining attenuation performance, material efficiency, and manufacturing constraints. Experimental validation of the theoretical predictions represents a critical next step, particularly utilizing the structural materials analyzed in Appendix C (aluminum alloys and carbon/epoxy composites). Such experimental campaigns would validate the universal geometric performance principles across the $150\times$ stiffness variation demonstrated analytically, while addressing practical considerations including manufacturing tolerances, boundary condition effects, and damping characteristics in real engineering materials. The demonstrated frequency scaling relationships ($f \propto \sqrt{D/\rho h}$) provide clear guidelines for specimen design and testing protocols across different material systems. Additionally, the integration of the Wave Finite Element (WFE) method presents particularly promising opportunities for analyzing finite metamaterial plates with superior computational efficiency. The WFE approach, which combines finite element discretization of unit cells with wave propagation analysis, could dramatically reduce computational costs compared to conventional FEM by exploiting the periodic nature of the structures. This method would enable efficient analysis of large-scale finite plates while maintaining the accuracy demonstrated by the PWE/EPWE framework for infinite structures. Furthermore, spectral element approaches and machine learning-assisted optimization could complement the WFE methodology to accelerate the design process and unlock new possibilities for real-time optimization and

⁹⁷⁶ adaptive metamaterial systems.

⁹⁷⁷ **Acknowledgments**

⁹⁷⁸ The authors acknowledge the support of the Brazilian National Council for
⁹⁷⁹ Scientific and Technological Development (CNPq, Grant Nos. 157159/2013-
⁹⁸⁰ 2, 403234/2021-2, 405638/2022-1, 404417/2024-8, and 305286/2025-0), the Co-
⁹⁸¹ ordination for the Improvement of Higher Education Personnel (CAPES, Fi-
⁹⁸² nance Code 001), the Maranhão State Research Foundation (FAPEMA, Grant
⁹⁸³ No. APP-01842/25), and the São Paulo Research Foundation (FAPESP, Grant
⁹⁸⁴ No. 2018/15894-0). The authors also thank the Federal Institute of Maranhão
⁹⁸⁵ (IFMA) and the Vale Institute of Technology (ITV) for institutional support.

986 **Appendix A. PWE Matrix Formulation for LRSC Plates with Five**
 987 **Lattice Configurations**

988 This appendix details the matrix formulation required for PWE computational
 989 implementation across five lattice configurations. Starting from the governing
 990 equation presented in Section 2.1 (Eq. 1) with resonator forces at lattice posi-
 991 tions \mathbf{R} and local positions \mathbf{r}_j , the displacement field follows Bloch's theorem
 992 with plane wave expansion as defined in Eq. (7): $w(\mathbf{r}) = \sum_{\mathbf{G}} w(\mathbf{G}) e^{i(\mathbf{k} + \mathbf{G}) \cdot \mathbf{r}}$,
 993 where \mathbf{G} are reciprocal lattice vectors, \mathbf{k} is the Bloch wave vector, and $w(\mathbf{G})$
 994 are plane wave amplitudes.

995 The resonator forces follow Eq. (2) with complex dynamic stiffness:

$$p_j(\mathbf{r}_j + \mathbf{R}) = k_j^* [u_j(\mathbf{r}_j + \mathbf{R}) - w(\mathbf{r}_j + \mathbf{R})] \quad (\text{A.1})$$

996 where $k_j^* = k_j(1 + i\eta_j)$ incorporates resonator damping effects as established
 997 in Section 2.1, with $k_j = m_j \omega_j^2$ being the resonator stiffness, u_j the resonator
 998 displacement, and η_j the loss factor.

999 Applying the plane wave expansion to the governing equation and utilizing or-
 1000 thogonality of exponential functions yields the matrix eigenvalue problem:

$$[\mathbf{K} - \omega^2 \mathbf{M}] \{ \mathbf{q} \} = \mathbf{0} \quad (\text{A.2})$$

1001 where $\mathbf{q} = [\mathbf{w}^T, \mathbf{u}^T]^T$ contains both plate wave amplitudes $\mathbf{w} = [w(\mathbf{G}_1), w(\mathbf{G}_2), \dots, w(\mathbf{G}_{N_g})]^T$
 1002 and resonator displacements $\mathbf{u} = [u_1, u_2, \dots, u_{N_j}]^T$, with $N_g = (2M+1)^2$ plane
 1003 waves.

1004 The augmented system matrices are assembled as:

$$\begin{bmatrix} \mathbf{K}_{pp} + \mathbf{K}_r & -\mathbf{PK}_j \\ -\mathbf{K}_j \mathbf{P}^T & \mathbf{K}_j \end{bmatrix} \begin{bmatrix} \mathbf{w} \\ \mathbf{u} \end{bmatrix} = \omega^2 \begin{bmatrix} \mathbf{M}_{pp} & \mathbf{0} \\ \mathbf{0} & \mathbf{M}_{rr} \end{bmatrix} \begin{bmatrix} \mathbf{w} \\ \mathbf{u} \end{bmatrix} \quad (\text{A.3})$$

1005 where \mathbf{K}_{pp} and \mathbf{M}_{pp} are the plate stiffness and mass matrices, $\mathbf{K}_j = \text{diag}(k_1^*, k_2^*, \dots, k_{N_j}^*)$
 1006 contains resonator stiffnesses, $\mathbf{M}_{rr} = \text{diag}(m_{r,1}, m_{r,2}, \dots, m_{r,N_j})$ contains res-
 1007 onator masses with $m_j = \gamma \rho S h / N_j$, and \mathbf{P} is the coupling matrix with elements
 1008 $P_{i,j} = e^{i\mathbf{G}_i \cdot \mathbf{r}_j}$.

1009 The diagonal elements of the plate matrices are computed as:

$$\mathbf{K}_{pp}[i, i] = D \cdot S \cdot |\mathbf{k} + \mathbf{G}_i|^4 = D \cdot S \cdot [(k_x + G_{x,i})^2 + (k_y + G_{y,i})^2]^2 , \quad (\text{A.4})$$

$$\mathbf{M}_{pp}[i, i] = \rho h S . \quad (\text{A.5})$$

1010 The coupling matrix has elements $P_{i,j} = e^{i\mathbf{G}_i \cdot \mathbf{r}_j}$ and the resonator coupling
1011 stiffness matrix is $\mathbf{K}_r = \sum_{j=1}^{N_j} (k_j^*/S) \mathbf{P}_j \mathbf{P}_j^T$.

1012 Reciprocal lattice vectors \mathbf{G}_{mn} for indices $m, n \in [-M, M]$ are generated as:

$$\text{Square/Rectangular: } \mathbf{G}_{mn} = \frac{2\pi}{a_1} m \mathbf{e}_1 + \frac{2\pi}{a_2} n \mathbf{e}_2 \quad (\text{A.6})$$

$$\text{Triangular: } \mathbf{G}_{mn} = \frac{2\pi}{a} m \mathbf{e}_1 + \frac{2\pi}{a} \frac{m - 2n}{\sqrt{3}} \mathbf{e}_2 \quad (\text{A.7})$$

$$\text{Hexagonal: } \mathbf{G}_{mn} = \frac{2\pi}{a\sqrt{3}} (m - n) \mathbf{e}_1 + \frac{2\pi}{3a} (m + n) \mathbf{e}_2 \quad (\text{A.8})$$

$$\text{Kagomé: } \mathbf{G}_{mn} = \frac{\pi}{a} (m - n) \mathbf{e}_1 + \frac{\pi}{a} \frac{m + n}{\sqrt{3}} \mathbf{e}_2 \quad (\text{A.9})$$

1013 Unit cell areas and resonator configurations: square/rectangular/triangular $N_j =$
1014 1 with $\mathbf{r}_1 = \mathbf{0}$, areas $S = a^2, a_1 a_2, a^2 \sqrt{3}/2$ respectively; hexagonal $N_j = 2$ with
1015 $\mathbf{r}_{1,2} = (0, \pm a/2)$, area $S = 3a^2 \sqrt{3}/2$; kagomé $N_j = 3$ with $\mathbf{r}_1 = (-a/2, -a\sqrt{3}/6),$
1016 $\mathbf{r}_2 = (a/2, -a\sqrt{3}/6), \mathbf{r}_3 = (0, a\sqrt{3}/3)$, area $S = 2a^2 \sqrt{3}$.

1017 Computational implementation: generate $(2M + 1)^2$ reciprocal vectors using
1018 Eqs. (A.6)-(A.9), compute diagonal plate matrices via Eqs. (A.4)-(A.5), as-
1019 semble coupling matrix \mathbf{P} with phase factors $e^{i\mathbf{G}_i \cdot \mathbf{r}_j}$, form augmented system
1020 Eq. (A.3), solve eigenvalue problem, and extract physical frequencies.

1021 Matrix assembly algorithm for each wave vector \mathbf{k} : (1) Initialize sparse matrices
1022 $\mathbf{A}_n, \mathbf{A}_d \in \mathbb{C}^{(N_g + N_j) \times (N_g + N_j)}$ with $N_g = (2M + 1)^2$; (2) Fill diagonal blocks:
1023 $\mathbf{A}_n[1 : N_g, 1 : N_g] = \mathbf{M}_{pp}, \mathbf{A}_d[1 : N_g, 1 : N_g] = \mathbf{K}_{pp}$; (3) For each resonator j :
1024 compute phase vector \mathbf{p}_j with $[\mathbf{p}_j]_i = e^{i\mathbf{G}_i \cdot \mathbf{r}_j}$, add coupling $\mathbf{A}_d[1 : N_g, 1 : N_g] \leftarrow$
1025 $\mathbf{A}_d[1 : N_g, 1 : N_g] + (k_j^*/S) \mathbf{p}_j \mathbf{p}_j^H$, set off-diagonal coupling $\mathbf{A}_d[1 : N_g, N_g + j] =$
1026 $-k_j^* \mathbf{p}_j$, $\mathbf{A}_d[N_g + j, 1 : N_g] = -k_j^* \mathbf{p}_j^H$, and diagonal terms $\mathbf{A}_n[N_g + j, N_g + j] =$
1027 $m_{r,j}$, $\mathbf{A}_d[N_g + j, N_g + j] = k_j^*$.

1028 Eigenvalue solution: $\mathbf{A}_d\phi_i = \lambda_i \mathbf{A}_n\phi_i$ yields frequencies $f_i = \text{Re}(\sqrt{|\lambda_i|})/(2\pi)$.

1029 Computational parameters: typical $M = 3 - 5$ plane waves per direction provide

1030 convergence for $|\mathbf{k} + \mathbf{G}_{\max}|a < \pi$. For bare plates: $\omega^2 = (D/\rho h)|\mathbf{k} + \mathbf{G}_i|^4$ directly.

Table A.12: Summary of lattice-specific parameters for PWE implementation

Lattice	Unit Cell Area	Resonators/Cell	Key FIBZ Points
Square	a^2	1	$\Gamma(0,0), X(\pi/a,0), M(\pi/a,\pi/a)$
Rectangular	$a_x a_y$	1	$\Gamma(0,0), X(\pi/a_x,0), M(\pi/a_x,\pi/a_y)$
Triangular	$a^2 \sqrt{3}/2$	1	$\Gamma(0,0), X(4\pi/3a,0), M(\pi/a,\pi/(a\sqrt{3}))$
Honeycomb	$3a^2 \sqrt{3}/2$	2	$\Gamma(0,0), X(4\pi/(3a\sqrt{3}),0), M(\pi/(a\sqrt{3}),\pi/(3a))$
Kagomé	$2a^2 \sqrt{3}$	3	$\Gamma(0,0), X(2\pi/(3a),0), M(\pi/(2a),\pi/(2a\sqrt{3}))$

1031 **Appendix B. EPWE Matrix Formulation for Complex Wave Vector
1032 Analysis**

1033 This appendix details the Extended PWE (EPWE) matrix formulation for com-
1034 puting complex wave vectors $k(\omega)$ at prescribed frequencies. The method solves
1035 the inverse eigenvalue problem, enabling direct analysis of wave attenuation and
1036 evanescent modes within bandgaps.

1037 Starting from the same governing equation (Eq. 1), EPWE maintains the Bloch
1038 expansion but reformulates the problem as a polynomial eigenvalue equation in
1039 k . The displacement field retains the form $w(\mathbf{r}) = \sum_{\mathbf{G}} w(\mathbf{G}) e^{i(\mathbf{k} + \mathbf{G}) \cdot \mathbf{r}}$ where
1040 $\mathbf{k} = k_r + ik_i \in \mathbb{C}$ allows exponentially decaying modes.

1041 For wave propagation direction $\mathbf{k} = k(\cos \phi, \sin \phi)$, the governing equation yields
1042 a quartic polynomial eigenvalue problem:

$$[\mathbf{A}_3 k^3 + \mathbf{A}_2 k^2 + \mathbf{A}_1 k + \mathbf{A}_0] \psi = \mathbf{0} \quad (\text{B.1})$$

1043 where coefficient matrices depend on lattice geometry, frequency, and resonator
1044 coupling.

1045 The coefficient matrices for each reciprocal vector \mathbf{G}_i are constructed as:

$$\mathbf{A}_0[i, i] = \frac{DS}{a^4} |\mathbf{G}_i|^4 - \rho h S \omega^2 + D_j(\omega) \quad (\text{B.2})$$

$$\mathbf{A}_1[i, i] = \frac{4DS}{a^4} |\mathbf{G}_i|^2 (\mathbf{G}_i \cdot \hat{\mathbf{k}}) \quad (\text{B.3})$$

$$\mathbf{A}_2[i, i] = \frac{2DS}{a^4} [|\mathbf{G}_i|^2 + 2(\mathbf{G}_i \cdot \hat{\mathbf{k}})^2] \quad (\text{B.4})$$

$$\mathbf{A}_3[i, i] = \frac{4DS}{a^4} (\mathbf{G}_i \cdot \hat{\mathbf{k}}) \quad (\text{B.5})$$

1046 where $\hat{\mathbf{k}} = (\cos \phi, \sin \phi)$ is the propagation direction and $D_j(\omega) = k_j^* - (k_j^*)^2 / (k_j^* -$
1047 $\omega^2 m_{r,j})$ is the frequency-dependent dynamic stiffness from Eq. (12).

1048 Companion matrix linearization transforms Eq. (B.1) into the generalized eigen-

1049 value problem:

$$\begin{bmatrix} -\mathbf{A}_3 & -\mathbf{A}_2 & -\mathbf{A}_1 & -\mathbf{A}_0 \\ \mathbf{I} & \mathbf{0} & \mathbf{0} & \mathbf{0} \\ \mathbf{0} & \mathbf{I} & \mathbf{0} & \mathbf{0} \\ \mathbf{0} & \mathbf{0} & \mathbf{I} & \mathbf{0} \end{bmatrix} \begin{bmatrix} \psi_1 \\ \psi_2 \\ \psi_3 \\ \psi_4 \end{bmatrix} = k \begin{bmatrix} \mathbf{I} & \mathbf{0} & \mathbf{0} & \mathbf{0} \\ \mathbf{0} & \mathbf{0} & \mathbf{0} & \mathbf{0} \\ \mathbf{0} & \mathbf{0} & \mathbf{0} & \mathbf{0} \\ \mathbf{0} & \mathbf{0} & \mathbf{0} & \mathbf{0} \end{bmatrix} \begin{bmatrix} \psi_1 \\ \psi_2 \\ \psi_3 \\ \psi_4 \end{bmatrix} \quad (\text{B.6})$$

1050 Computational algorithm: (1) For each frequency ω , compute coefficient matrices using Eqs. (B.2)-(B.5) with the same reciprocal vectors from Appendix A; (2)
1051 Assemble companion matrix Eq. (B.6) of size $4N_g \times 4N_g$ with $N_g = (2M + 1)^2$;
1052 (3) Solve eigenvalue problem to extract $4N_g$ complex wave vectors k_i ; (4) Apply
1053 eigenvector tracking for mode continuity across frequency; (5) Normalize results:
1054 $k_{\text{norm}} = k \cdot a / (2\pi)$.

1055 Physical interpretation: $\text{Re}(k)$ represents propagating modes while $\text{Im}(k) > 0$
1056 quantifies evanescent decay. The attenuation constant $\mu = \text{Im}(k) \cdot a$ [Np/cell]
1057 directly measures wave attenuation within bandgaps. Typical computational
1058 parameters: $M = 2 - 3$ plane waves provide convergence for EPWE due to
1059 polynomial scaling, with frequency resolution $\Delta f = 1 - 10$ [Hz] depending on
1060 application requirements.
1061

1062 **Appendix C. Extension to Structural Materials - Multi-Scale Anal-**
1063 **ysis**

1064 While this study focuses on polymeric materials for practical validation through
1065 rapid prototyping, the PWE/EPWE methodology developed is applicable to a
1066 broad range of structural materials. This condensed appendix demonstrates the
1067 universality of our framework across aluminum and carbon/epoxy materials, con-
1068 firming that geometric performance advantages represent material-independent
1069 design principles. Only essential findings are presented to maintain manuscript
1070 conciseness while addressing material generalizability.

1071 *Appendix C.1. Material Properties and Scaling Analysis*

1072 Three materials spanning $150\times$ stiffness variation are analyzed: Vero White Plus
1073 polymer (baseline), aluminum 6061 [46], and carbon/epoxy composite [64].

1074 Table C.13 presents the comparative material properties used in this multi-
1075 material analysis:

Table C.13: Comparative material properties for multi-material analysis

Material	E [GPa]	ρ [kg/m ³]	ν	D [N·m]	D/D _{polymer}
Vero White Plus	0.86	600	0.36	6.59×10^{-1}	1.0
Aluminum 6061	70	2700	0.30	5.13×10^1	77.9
Carbon/Epoxy UD	135	1580	0.30	9.89×10^1	150.1

1076 *Appendix C.2. Frequency Scaling and Key Results*

1077 Frequency scaling follows $f_{B_1} \propto \sqrt{D/\rho h}$, shifting operational ranges proportion-
1078 ally while preserving geometric performance hierarchies. Table C.14 summarizes
1079 the operational frequency ranges for each material:

1080 *Appendix C.3. PWE Analysis Results for Alternative Materials*

1081 Using identical PWE computational parameters ($M = 3$, convergence tolerance
1082 10^{-6}), the band gap analysis was extended to aluminum and carbon/epoxy

Table C.14: Frequency scaling and operational ranges across materials

Material	h [mm]	a [mm]	h/a	Target Range [Hz]	f_B [Hz]
Vero White Plus	2.0	100	0.02	10–200	116
Aluminum 6061	2.0	100	0.02	150–725	484
Carbon/Epoxy UD	2.0	100	0.02	300–1200	879

¹⁰⁸³ configurations. The methodology maintains numerical stability across the $150 \times$
¹⁰⁸⁴ stiffness variation, confirming the robustness of the semi-analytical approach.

¹⁰⁸⁵ *Appendix C.3.1. Aluminum Analysis (150-725 Hz Range)*

¹⁰⁸⁶ Table C.15 presents the complete band gap width analysis for aluminum lattices
¹⁰⁸⁷ across selected resonator frequencies, including the Bragg frequency (484 Hz):

¹⁰⁸⁸ *Appendix C.3.2. Carbon/Epoxy Analysis (300-1200 Hz Range)*

¹⁰⁸⁹ Table C.16 presents the complete band gap width analysis for carbon/epoxy
¹⁰⁹⁰ lattices across selected resonator frequencies, including the Bragg frequency (879
¹⁰⁹¹ Hz):

Table C.15: Full band gap width evolution for Aluminum 6061 lattices with FBGW 1 and FBGW 2 for multi-resonator configurations (material properties from Xiao et al. [46]; all FBGW values in Hz; bold: maximum FBGW; -: no bandgap; $f_B = 484$ Hz for square lattice).

f_j (Hz)	Square FBGW	Rectangular FBGW	Triangular FBGW	Honeycomb FBGW 1	Honeycomb FBGW 2	Kagomé FBGW 1	Kagomé FBGW 2
150	36.1	33.7	36.4	35.8	-	26.3	-
175	43.2	39.2	43.8	42.5	-	16.9	10.7
200	50.4	44.9	51.2	49.2	20.8	13.3	18.8
225	57.9	50.7	59.0	55.7	45.0	12.3	20.0
250	66.4	56.0	68.1	57.7	66.5	12.5	19.9
275	75.8	61.1	78.3	43.3	66.7	13.4	19.5
300	84.2	66.9	87.4	26.8	68.0	14.7	19.6
325	91.4	69.0	96.0	11.5	70.3	16.3	20.5
350	97.3	58.6	103.7	-	73.5	18.4	22.1
375	113.4	81.4	120.9	-	77.4	11.7	24.2
400	107.0	30.4	127.5	-	81.9	3.8	26.9
425	131.1	74.7	145.8	-	87.0	-	26.6
450	111.0	5.4	161.7	-	92.7	-	23.1
475	111.0	30.7	172.1	-	98.9	-	20.0
484 ^a	107.0	22.9	176.9	-	101.2	-	19.1
500	89.9	-	198.4	-	105.3	-	17.8
525	89.9	-	198.4	-	111.1	-	16.5
575	71.7	-	222.0	-	113.7	-	16.4
625	56.2	-	219.4	-	93.6	-	17.5
725	31.5	-	196.1	-	62.9	-	17.4

^aBragg frequency for square lattice configuration.

The comparative analysis across aluminum and carbon/epoxy materials reveals consistent lattice performance hierarchy. Tables C.15 and C.16 demonstrate that triangular lattices achieve superior relative bandwidth (40-42%) across all materials spanning 150× stiffness variation, validating that geometric advantages represent material-independent design principles. The frequency scaling

Table C.16: Full band gap width evolution for Carbon/Epoxy UD lattices with FBGW 1 and FBGW 2 for multi-resonator configurations (material properties from CMH-17 [64]; all FBGW values in Hz; bold: maximum FBGW; -: no bandgap; $f_B = 879$ Hz for square lattice).

f_j (Hz)	Square FBGW	Rectangular FBGW	Triangular FBGW	Honeycomb FBGW 1	Honeycomb FBGW 2	Kagomé FBGW 1	Kagomé FBGW 2
300	73.1	67.4	73.9	72.3	-	35.9	10.4
350	87.1	78.5	88.3	85.9	25.6	25.4	32.4
400	102.9	89.8	104.9	99.0	73.3	22.5	36.2
450	119.3	103.2	124.2	105.2	120.7	22.7	36.1
500	136.6	111.9	140.9	78.1	121.1	24.3	35.4
550	154.7	118.0	158.3	45.2	123.9	26.9	35.7
600	174.0	133.0	182.3	14.9	128.8	30.4	37.7
650	191.4	136.7	201.5	-	135.5	30.3	41.2
700	207.8	126.3	220.3	-	143.8	15.3	45.9
750	231.8	151.7	253.7	-	153.5	-	51.5
800	231.5	110.2	279.5	-	164.4	-	44.2
850	207.3	66.4	305.9	-	176.4	-	37.7
879 ^a	194.1	41.2	321.2	-	183.8	-	34.7
900	164.4	-	334.0	-	189.2	-	32.9
950	164.4	-	358.6	-	201.1	-	30.1
1000	134.2	-	381.8	-	210.8	-	29.3
1050	108.4	-	402.0	-	203.8	-	29.9
1100	112.2	-	408.1	-	183.1	-	31.0
1150	88.7	-	398.4	-	164.3	-	32.0
1200	84.2	-	389.8	-	147.4	-	32.5

^aBragg frequency for square lattice configuration.

¹⁰⁹⁷ preserves this hierarchy while shifting operational ranges proportionally to material stiffness ($\sqrt{D/\rho h}$), confirming PWE methodology robustness across the ¹⁰⁹⁸ entire structural material spectrum studied. ¹⁰⁹⁹

1100 Appendix D. Framework for Lattice Selection in Engineering Applications

Table D.17 provides a quantitative framework for lattice selection based on the comparative analysis presented in Sections 3 and 4.1.

Table D.17: Lattice selection framework for engineering applications.

Metric	Kagomé	Honeycomb	Triangular	Square	Rectangular
Peak Atten. [dB]	-292.65	-220.33	-174.19	-173.09	-129.93
Material Eff. (m_{ratio})	1.00 (ref.)	0.58	0.25	0.29	0.14
Optimal Application	Max. vibration suppression	Dual-freq. control	Broadband control	Standard control	Directional control

Appendix D.1. Application-Specific Guidelines

1105 Recommended lattice configurations for specific engineering scenarios:

- **Critical vibration isolation** (precision instrumentation, sensitive equipment): Kagomé (maximum attenuation -292.65 dB) or honeycomb (manufacturing advantages).
 - **Broadband noise control** (automotive panels, aerospace structures): Triangular (superior bandwidth, 25% material efficiency) or square (standard performance).
 - **Multi-frequency applications** (industrial machinery, HVAC systems): Honeycomb (dual band gaps) or kagomé (multi-resonator capability).
 - **Constrained design space** (architectural integration, retrofit): Rectangular (directional control) or square (space-efficient).

1116 **References**

- 1117 [1] M. Mir, F. Nasirzadeh, S. Lee, D. Cabrera, A. Mills, Construction noise
1118 management: A systematic review and directions for future research,
1119 Applied Acoustics 197 (2022) 108936. doi:10.1016/j.apacoust.2022.
1120 108936.
- 1121 [2] R. Kandasamy, F. Cui, N. Townsend, C. C. Foo, J. Guo, A. Shenoi,
1122 Y. Xiong, A review of vibration control methods for marine offshore struc-
1123 tures, Ocean Engineering 127 (2016) 279–297. doi:10.1016/j.oceaneng.
1124 2016.10.001.
- 1125 [3] M. D. Rao, Recent applications of viscoelastic damping for noise control
1126 in automobiles and commercial airplanes, Journal of Sound and Vibration
1127 262 (3) (2003) 457–474. doi:10.1016/S0022-460X(03)00106-8.
- 1128 [4] J. Masri, M. Amer, S. Salman, M. Ismail, M. Elsisi, A survey of mod-
1129 ern vehicle noise, vibration, and harshness: A state-of-the-art, Ain Shams
1130 Engineering Journal 15 (10) (2024) 102957. doi:10.1016/j.asej.2024.
1131 102957.
- 1132 [5] K. H. Matlack, A. Bauhofer, S. Krödel, A. Palermo, C. Daraio, Compos-
1133 ite 3d-printed metastructures for low-frequency and broadband vibration
1134 absorption, Proceedings of the National Academy of Sciences 113 (2016)
1135 8386–8390. doi:10.1073/pnas.1600171113.
- 1136 [6] X. An, C. Lai, H. Fan, C. Zhang, 3d acoustic metamaterial-based me-
1137 chanical metalattice structures for low-frequency and broadband vibration
1138 attenuation, International Journal of Solids and Structures 191-192 (2020)
1139 293–306. doi:10.1016/j.ijsolstr.2020.01.020.
- 1140 [7] G. Comandini, C. Khodr, V. P. Ting, M. Azarpeyvand, F. Scarpa, Archi-
1141 tected acoustic metamaterials: An integrated design perspective, Applied
1142 Physics Reviews 12 (1) (2024) 011340. doi:10.1063/5.0230888.

- 1143 [8] S. Lin, Y. Zhang, Y. Liang, Y. Liu, C. Liu, Z. Yang, Bandgap characteristics
1144 and wave attenuation of metamaterials based on negative-stiffness dynamic
1145 vibration absorbers, *Journal of Sound and Vibration* 502 (2021) 116088.
1146 doi:10.1016/j.jsv.2021.116088.
- 1147 [9] L. D'Alessandro, R. Ardito, F. Braghin, A. Corigliano, Low frequency 3d
1148 ultra-wide vibration attenuation via elastic metamaterial, *Scientific Reports* 9 (2019) 8039. doi:10.1038/s41598-019-44507-6.
- 1150 [10] M. I. Hussein, M. J. Leamy, M. Ruzzene, Dynamics of phononic materials
1151 and structures: Historical origins, recent progress, and future outlook, *Applied Mechanics Reviews* 66 (4) (2014) 040802. doi:10.1115/1.4026911.
- 1153 [11] L. E. Kinsler, A. R. Frey, A. B. Coppens, J. V. Sanders, *Fundamentals of
1154 Acoustics*, 4th Edition, Wiley, 2000.
- 1155 [12] S. Kumar, H. P. Lee, Recent advances in acoustic metamaterials for simul-
1156 taneous sound attenuation and air ventilation performances, *Crystals* 10 (8)
1157 (2020) 686. doi:10.3390/cryst10080686.
- 1158 [13] M. Weiner, X. Ni, M. Li, A. Alù, A. B. Khanikaev, Demonstration of a
1159 third-order hierarchy of topological states in a three-dimensional acoustic
1160 metamaterial, *Science Advances* 6 (13) (2020) eaay4166. doi:10.1126/
1161 sciadv.aay4166.
- 1162 [14] L. Lu, T. Yamamoto, M. Otomori, T. Yamada, K. Izui, S. Nishiwaki, Topol-
1163 ogy optimization of an acoustic metamaterial with negative bulk modulus
1164 using local resonance, *Finite Elements in Analysis and Design* 72 (2013)
1165 1–12. doi:10.1016/j.finel.2013.04.005.
- 1166 [15] D. Li, L. Zigoneanu, B.-I. Popa, S. A. Cummer, Design of an acoustic
1167 metamaterial lens using genetic algorithms, *The Journal of the Acoustical
1168 Society of America* 132 (4) (2012) 2823–2833. doi:10.1121/1.4744942.

- 1169 [16] E. Yablonovitch, Inhibited spontaneous emission in solid-state physics and
1170 electronics, *Physical Review Letters* 58 (20) (1987) 2059–2062. doi:10.
1171 1103/PhysRevLett.58.2059.
- 1172 [17] S. John, Strong localization of photons in certain disordered dielectric
1173 superlattices, *Physical Review Letters* 58 (23) (1987) 2486–2489. doi:
1174 10.1103/PhysRevLett.58.2486.
- 1175 [18] R. D. Meade, K. D. Brommer, A. M. Rappe, J. D. Joannopoulos, Existence
1176 of a photonic band gap in two dimensions, *Applied Physics Letters* 61 (4)
1177 (1992) 495–497. doi:10.1063/1.107868.
- 1178 [19] P. R. Villeneuve, M. Piché, Photonic band gaps in two-dimensional square
1179 and hexagonal lattices, *Physical Review B* 46 (8) (1992) 4969–4973. doi:
1180 10.1103/PhysRevB.46.4969.
- 1181 [20] J. D. Joannopoulos, P. R. Villeneuve, S. Fan, Photonic crystals: Putting
1182 a new twist on light, *Nature* 386 (6621) (1997) 143–149. doi:10.1038/
1183 386143a0.
- 1184 [21] M. M. Sigalas, E. N. Economou, Elastic and acoustic wave band structure,
1185 *Journal of Sound and Vibration* 158 (2) (1992) 377–382. doi:10.1016/
1186 0022-460X(92)90059-7.
- 1187 [22] M. S. Kushwaha, P. Halevi, G. Martinez, L. Dobrzynski, B. Djafari-
1188 Rouhani, Theory of acoustic band structure of periodic elastic composites,
1189 *Physical Review B* 49 (4) (1994) 2313–2322. doi:10.1103/PhysRevB.49.
1190 2313.
- 1191 [23] J. O. Vasseur, B. Djafari-Rouhani, L. Dobrzynski, M. S. Kushwaha,
1192 P. Halevi, Band-gap engineering in periodic elastic composites, *Applied
1193 Physics Letters* 64 (9) (1994) 1085–1087. doi:10.1063/1.110940.
- 1194 [24] J.-O. Vasseur, P. A. Deymier, B. Djafari-Rouhani, Y. Pennec, A.-C. Hladky-
1195 Hennion, Absolute forbidden bands and waveguiding in two-dimensional

- phononic crystal plates, Physical Review B 77 (8) (2008) 085415. doi:
10.1103/PhysRevB.77.085415.
- [25] Y. Pennec, J.-O. Vasseur, B. Djafari-Rouhani, Two-dimensional phononic crystals: Examples and applications, Surface Science Reports 65 (8) (2010) 229–291. doi:10.1016/j.surfrep.2010.08.002.
- [26] G. Floquet, Sur les équations différentielles linéaires à coefficients périodiques, Annales scientifiques de l’École normale supérieure 12 (1883) 47–88.
- [27] F. Bloch, Über die quantenmechanik der elektroden, Zeitschrift für Physik 52 (1928) 555–600. doi:10.1007/BF01339455.
- [28] L. Brillouin, Wave Propagation in Periodic Structures, McGraw-Hill, 1946.
- [29] Y. El Hassouani, C. Li, Y. Pennec, E. H. El Boudouti, H. Larabi, A. Akjouj, O. Bou Matar, V. Laude, N. Papanikolaou, Dual phononic and photonic band gaps in a periodic array of pillars deposited on a thin plate, Physical Review B 82 (15) (2010) 155405. doi:10.1103/PhysRevB.82.155405.
- [30] V. Laude, Phononic Crystals: Artificial Crystals for Sonic, Acoustic, and Elastic Waves, De Gruyter, 2015.
- [31] M. I. Hussein, Reduced bloch mode expansion for periodic media band structure calculations, Proceedings of the Royal Society A 462 (2073) (2006) 3385–3408. doi:10.1098/rspa.2008.0471.
- [32] S. Zhang, J. H. Wu, Z. Hu, Low-frequency locally resonant band-gaps in phononic crystal plates with periodic spiral resonators, Journal of Applied Physics 113 (16) (2013) 163511. doi:10.1063/1.4803075.
- [33] Z. Liu, X. Zhang, Y. Mao, Y. Y. Zhu, Z. Yang, C. T. Chan, P. Sheng, Locally resonant sonic materials, Science 289 (5485) (2000) 1734–1736. doi:10.1126/science.289.5485.1734.

- 1222 [34] G. Wang, X. Wen, J. Wen, L. Shao, Y. Liu, Two-dimensional locally res-
1223 onant phononic crystals with binary structures, Physical Review Letters
1224 93 (15) (2004) 154302. doi:[10.1103/PhysRevLett.93.154302](https://doi.org/10.1103/PhysRevLett.93.154302).
- 1225 [35] G. Wang, X. Wen, J. Wen, Y. Liu, Quasi-one-dimensional periodic struc-
1226 ture with locally resonant band gap, Journal of Applied Mechanics 73 (1)
1227 (2005) 167–170. doi:[10.1115/1.2061947](https://doi.org/10.1115/1.2061947).
- 1228 [36] J.-C. Hsu, T.-T. Wu, Lamb waves in binary locally resonant phononic
1229 plates with two-dimensional lattices, Applied Physics Letters 90 (20) (2007)
1230 201904. doi:[10.1063/1.2739369](https://doi.org/10.1063/1.2739369).
- 1231 [37] M. Oudich, M. B. Assouar, Z. Hou, Propagation of acoustic waves and
1232 waveguiding in a two-dimensional locally resonant phononic crystal plate,
1233 Applied Physics Letters 97 (19) (2010) 193503. doi:[10.1063/1.3513218](https://doi.org/10.1063/1.3513218).
- 1234 [38] M. Oudich, M. Senesi, M. B. Assouar, M. Ruzenne, J.-H. Sun, B. Vincent,
1235 Z. Hou, T.-T. Wu, Experimental evidence of locally resonant sonic band
1236 gap in two-dimensional phononic stubbed plates, Physical Review B 84 (16)
1237 (2011) 165136. doi:[10.1103/PhysRevB.84.165136](https://doi.org/10.1103/PhysRevB.84.165136).
- 1238 [39] G. Kirchhoff, On the theory of elastic plates, Annalen der Physik 147 (1850)
1239 423–435.
- 1240 [40] A. E. H. Love, The small free vibrations and deformations of a thin elastic
1241 shell, Philosophical Transactions of the Royal Society A 179 (1888) 491–
1242 549.
- 1243 [41] R. D. Mindlin, Influence of rotatory inertia and shear on flexural motions
1244 of isotropic elastic plates, Journal of Applied Mechanics 18 (1951) 31–38.
1245 doi:[10.1115/1.4010217](https://doi.org/10.1115/1.4010217).
- 1246 [42] E. Reissner, The effect of transverse shear deformation on the bending
1247 of elastic plates, Journal of Applied Mechanics 12 (1945) 69–77. doi:[10.1115/1.4009435](https://doi.org/10.1115/1.4009435).

- 1249 [43] A. S. Phani, J. Woodhouse, N. A. Fleck, Wave propagation in two-
1250 dimensional periodic plates, *Journal of the Acoustical Society of America*
1251 119 (2006) 1995–2005. doi:[10.1121/1.2179748](https://doi.org/10.1121/1.2179748).
- 1252 [44] S.-T. Hsue, D.-M. Fang, S.-F. Tzeng, Extended plane-wave-expansion
1253 method for phononic crystals, *Physical Review B* 72 (2005) 085123. doi:
1254 [10.1103/PhysRevB.72.195118](https://doi.org/10.1103/PhysRevB.72.195118).
- 1255 [45] V. Laude, Y. Achaoui, S. Benchabane, A. Khelif, Evanescent bloch waves
1256 and the complex band structure of phononic crystals, *Physical Review B*
1257 80 (9) (2009) 092301. doi:[10.1103/PhysRevB.80.092301](https://doi.org/10.1103/PhysRevB.80.092301).
- 1258 [46] Y. Xiao, J. Wen, X. Wen, Flexural wave band gaps in locally resonant thin
1259 plates with periodically attached spring-mass resonators, *Journal of Physics*
1260 D: Applied Physics 45 (19) (2012) 195401. doi:[10.1088/0022-3727/45/19/195401](https://doi.org/10.1088/0022-3727/45/19/195401).
- 1262 [47] Y. Xiao, J. Wen, L. Huang, X. Wen, Analysis and experimental realization
1263 of locally resonant phononic plates carrying a periodic array of beam-like
1264 resonators, *Journal of Physics D: Applied Physics* 47 (4) (2013) 045307.
1265 doi:[10.1088/0022-3727/47/4/045307](https://doi.org/10.1088/0022-3727/47/4/045307).
- 1266 [48] E. J. P. Miranda, E. D. Nobrega, A. H. R. Ferreira, J. M. C. Dos Santos,
1267 Flexural wave band gaps in a multi-resonator elastic metamaterial plate
1268 using kirchhoff-love theory, *Mechanical Systems and Signal Processing* 116
1269 (2019) 480–504. doi:[10.1016/j.ymssp.2018.06.059](https://doi.org/10.1016/j.ymssp.2018.06.059).
- 1270 [49] E. J. P. Miranda Jr., E. D. Nobrega, S. F. Rodrigues, C. Aranas Jr., J. M. C.
1271 Dos Santos, Wave attenuation in elastic metamaterial thick plates: Analytical,
1272 numerical and experimental investigations, *International Journal of Solids and Structures* 204-205 (2020) 138–152. doi:[10.1016/j.ijsolstr.2020.08.002](https://doi.org/10.1016/j.ijsolstr.2020.08.002).
- 1275 [50] S. Lee, M. Ruzzene, Wave propagation control in thin elastic plates using

- 1276 elastic metasurfaces, Journal of Sound and Vibration 340 (2015) 142–155.
1277 doi:[10.1016/j.jsv.2014.07.011](https://doi.org/10.1016/j.jsv.2014.07.011).
- 1278 [51] M. Yao, Y. Chen, G. Huang, Elastic metamaterial plates for flexural wave
1279 attenuation in aerospace applications, Applied Physics Letters 104 (2014)
1280 191903. doi:[10.1063/1.4878786](https://doi.org/10.1063/1.4878786).
- 1281 [52] B. Zouari, S. Guenneau, F. Zolla, Experimental demonstration of a two-
1282 dimensional elastic metamaterial barrier for vibration isolation, Physical
1283 Review Applied 10 (2018) 014021. doi:[10.1103/PhysRevApplied.10.014021](https://doi.org/10.1103/PhysRevApplied.10.014021).
- 1285 [53] T. Wang, W. Zhang, X. Wei, Design and characterization of passive acous-
1286 tic panels using locally resonant metamaterials, Applied Acoustics 159
1287 (2020) 107053. doi:[10.1016/j.apacoust.2019.107053](https://doi.org/10.1016/j.apacoust.2019.107053).
- 1288 [54] D. Torrent, A. Pujol, J. Sánchez-Dehesa, Acoustic metamaterials for sound
1289 focusing and active control application, New Journal of Physics 15 (2013)
1290 043046. doi:[10.1088/1367-2630/15/4/043046](https://doi.org/10.1088/1367-2630/15/4/043046).
- 1291 [55] O. Lera, F. Castañeda, F. Vasquez, Adaptive metamaterial plate with
1292 embedded piezoelectric shunts for vibration control, Smart Materials and
1293 Structures 28 (2019) 045013. doi:[10.1088/1361-665X/ab0421](https://doi.org/10.1088/1361-665X/ab0421).
- 1294 [56] K. Y. Lee, W. Jeon, Hierarchical phononic crystals for filtering multiple
1295 target frequencies of ultrasound, Scientific Reports 10 (2020) 8070. doi:
1296 [10.1038/s41598-020-64234-7](https://doi.org/10.1038/s41598-020-64234-7).
- 1297 [57] J. Jiang, X. Yang, Y. Hu, A novel auxetic acoustic metamaterial plate
1298 with tunable bandgap, Applied Physics Letters 121 (8) (2022) 081702. doi:
1299 [10.1016/j.ijmecsci.2022.107414](https://doi.org/10.1016/j.ijmecsci.2022.107414).
- 1300 [58] V. F. Dal Poggetto, F. Bosia, M. Miniaci, N. M. Pugno, Band-gap enhance-
1301 ment in periodic frames using hierarchical structures, International Jour-
1302 nal of Solids and Structures 216 (2021) 68–82. doi:[10.1016/j.ijsolstr.2021.01.003](https://doi.org/10.1016/j.ijsolstr.2021.01.003).

- 1304 [59] N. Kumar, S. Pal, Low frequency and wide band gap metamaterial with
1305 divergent shaped star units: Numerical and experimental investigations,
1306 Applied Physics Letters 115 (25) (2019) 254101. doi:10.1063/1.5119754.
- 1307 [60] Q. Wang, J. Li, Y. Zhang, Y. Xue, F. Li, Bandgap properties in meta-
1308 material sandwich plate with periodically embedded plate-type resonators,
1309 Mechanical Systems and Signal Processing 151 (2021) 107375. doi:10.
1310 1016/j.ymssp.2020.107375.
- 1311 [61] Y. L. Gengwang Yan, Song Yao, Propagation of elastic waves in meta-
1312 material plates with various lattices for low-frequency vibration attenu-
1313 ation, Journal of Sound and Vibration 536 (2022) 117140. doi:<https://doi.org/10.1016/j.jsv.2022.117140>.
- 1315 [62] J. Li, X. Fan, F. Li, Numerical and experimental study of a sandwich-like
1316 metamaterial plate for vibration suppression, Composite Structures 238
1317 (2020) 111969. doi:10.1016/j.compstruct.2020.111969.
- 1318 [63] X.-S. Wei, Z. Wu, G. Yan, W. Zhang, Investigations on impedance mis-
1319 match and modal coupling in multilayer resonator metamaterial plates,
1320 Applied Acoustics 185 (2021) 108342. doi:10.1016/j.apacoust.2021.
1321 108342.
- 1322 [64] SAE International, Composite Materials Handbook-17, Volume 2: Polymer
1323 Matrix Composites Materials Properties, revision g Edition, SAE Interna-
1324 tional, Warrendale, PA, 2012, cMH-17-2G.